A&A 412, 669–687 (2003)
DOI: 10.1051/0004-6361:20031445

Astronomy & Astrophysics

NGC 5953/54: *BVRIHαJK* photometry and [N II] Fabry-Perot interferometry

I. The data⋆,⋆⋆

H. M. Hernández-Toledo[1], I. Fuentes-Carrera[1], M. Rosado[1], I. Cruz-González[1], A. Franco-Balderas[1], and D. Dultzin-Hacyan[1]

Instituto de Astronomía – UNAM – Apartado Postal 70-264, 04510 México D.F., México
e-mail: [margarit;irene;iqui;alfred;deborah]@astroscu.unam.mx

Received 14 April 2003 / Accepted 15 September 2003

Abstract. We present new *BVRIHαJK* imaging and [N II] scanning Fabry-Perot observations for the interacting galaxy pair NGC 5953/54. Morphology is reviewed using a combination of contrast-enhanced images, color-index maps, and geometric (radial μ, $\epsilon = 1 - b/a$, PA and a_4/a) profile parameters. Our data are complemented by archived *V*/*R*/*H* images from HST. The Seyfert 2 NGC 5953 shows an underlying featureless disk (≥1.5 kpc) in all the observed bands and traces of faint external fan-like features in Hα and [N II]. A compact flocculent spiral pattern (≤1.5 kpc), and a ∼60 pc bar-like central structure are also observed. The Liner galaxy NGC 5954 is an inclined and distorted spiral with a strong circumnuclear starburst region and star-forming regions throughout the disk. A tidal bridge or distorted arm appears to link the two galaxies, extending to the northwest as a linear feature (plume). NGC 5954 also shows blue filaments delineating bubble-like features on the north side of the nucleus where our Fabry-Perot observations reveal double emission line profiles. We derive *BVRIJK* magnitudes and surface brightness profiles for the galaxies. HST *V*/*R* and *H*-band surface brightness profiles are also presented for NGC 5953. Fabry-Perot observations yield an [N II] velocity field and rotation curves for the components. The observations coupled with results from a simulation atlas of tidal features allow us 1) to suggest a tentative geometry of the encounter in NGC 5953/54, and 2) to comment about a suspected secular transformation in NGC 5953/54 via the interaction process. A forthcoming paper is devoted to a more detailed analysis of our observations including HI synthesis observations and *n*-body numerical simulations.

Key words. galaxies: spiral – galaxies: structure – galaxies: photometry – galaxies: interactions – galaxies: fundamental parameters – galaxies: kinematics and dynamics

1. Introduction

The sample of mixed morphology (E+S) pairs, drawn from the Catalog of Isolated Pairs of Galaxies in the Northern Hemisphere (Karachentsev 1972), have been analyzed for its completeness, morphological content, global (optical and MID/FIR) emission properties, luminosity functions and HI content, showing distinct signature of increased star formation, perturbed kinematics and dynamics in the spiral components of these pairs due to interactions. The (E+S) pairs proved to be an appropriate sample for testing and setting limits on the ability of pre or non-merger interactions to initiate luminosity evolution in a local optically-selected sample (Hernández-Toledo et al. 1999, 2001, 2003). These results led us to start since 1999 systematic observations to obtain detailed photometry (optical and near-IR) and kinematics; Hα spectroscopy and Fabry-Perot interferometry with the aim of studying the processes of formation and evolution of galaxies in paired environments.

Among our first observational results on (E+S) pairs (cf. Franco-Balderas et al. 2003) and from other studies (cf. Domingue et al. 2003) a non-negligible fraction (∼15%) of AGNs in (E+S) pairs has been detected, suggesting that in addition to the star formation activity, nuclear activity in their inner regions may be triggered by an encounter with a close companion. Although some statistical studies have found an excess of companions in Seyfert 2 over field samples at a high significance level, e.g. Dahari (1984), Keel et al. (1985),

Send offprint requests to: H. M. Hernández-Toledo,
e-mail: hector@astroscu.unam.mx

⋆ Based on data obtained at the 1.5-m and 2.1-m telescopes of the Observatorio Astronomico Nacional, San Pedro Mártir, Baja California, México, operated by the Instituto de Astronomía, UNAM.

⋆⋆ Figures 5, 7, 10 and 13 are only available in electronic form at http://www.edpsciences.org

Table 1. Journal of observations.

Object	Telescope	Detector	Total field	Pixel size	Band	*FWHM*	Int. time	Sky level
			(arcmin)	(arcsec)		(arcsec)	(s)	(mag/arcsec^2)
NGC 5953/54	SPM 1.5-m	CCD Site 1024 × 1024	4.3′ × 4.3′	0.51	*B*	1.5	1800	21.95
				0.51	*V*	1.5	1200	20.85
				0.51	*R*	1.5	600	20.75
				0.51	*I*	1.5	600	19.42
				0.51	Hα	1.70	1200	
NGC 5953/54	SPM 2.1-m	Nicmos3 256 × 256	3.6′ × 3.6′	0.85	*J*	2.3	780	19.25
				0.85	*K*	2.2	900	17.7
NGC 5953/54	SPM 2.1-m	FP + CCD Tek 1024 × 1024	3′ × 3′	0.59	[N II]	1.65	2900	

Dultzin-Hacyan et al. (1999), these studies have proven less illuminating in telling whether AGN are really triggered by interactions, much less in telling how it happens physically, if indeed such triggering occurs.

In this paper, we emphasize that any connection between nuclear activity and interactions is likely to involve variables such as the geometry of the encounter and its role to control the fueling efficiency during the interaction, the intrinsic structure (bulge/disk mass ratio) of the intervening galaxies, the stage of the encounter and the time scales involved. We assume the hypothesis that if the excess of AGN due to triggering in galaxy pairs is mostly due to some particular mechanisms, these mechanisms might be more efficient in certain kind of encounters or at certain times (cf. Keel 1996). Since the (E+S) sample shows a wide range of separations, relative velocities and is plenty of morphological features, presumably associated to interactions, it is also reasonable to expect a wide range of encounter geometries in our sub-sample of paired AGNs. With the above assumptions in mind, in this paper we report the results of our observations for one such pair: NGC 5953/54.

NGC 5953/54 is a binary system where the galaxies are separated by a projected distance of 5.8 kpc and show clear signs of interaction in the form of a distorted morphology, the presence of prominent star-forming regions and a bridge connecting the two galaxies. Both galaxies show circumnuclear line emission associated with a recent burst of star formation. ROSAT observations of this pair, detect 1−5 keV emission associated with NGC 5953 (Henriksen & Cousineau 1999). The Seyfert 2 NGC 5953, was assumed as an early-type "S0/a" galaxy, while the Liner NGC 5954 is a late-type Scd galaxy thus forming an (S0/a + S) pair. The complex morphology shown at low resolution imaging lead Rampazzo et al. (1995) to describe this pair as an example of a significant cross fuelling event. More recently, Domingue et al. (2003) reported NGC 5953/54 as a cross fuelled Seyfert2 + Starburst, suggesting that perhaps interactions can both create and destroy spiral-like structures. An implicit idea thus far has been that NGC 5953 and NGC 5954 are interacting and perhaps with material being transferred. However, Jenkins (1984) modeled the encounter of NGC 5953/54 by using a two-body approximation similar to that in Toomre & Toomre (1972) finding no evidence of transfer of material.

In this first paper, we present the results of an homogeneous photometric optical-near-IR *BVRIHαJK* and kinematic [N II] Fabry-Perot study for the interacting pair NGC 5953/54 (KPG 468) with the aim of reviewing its multiwavelength morphology, photometric and kinematic properties. The results obtained are tentatively interpreted with the help of a simulation atlas of tidal features in galaxies (Howard et al. 1993) to suggest a plausible geometry of the encounter in NGC 5953/54 that could give some light on the AGN triggering process in pairs. The structure of the paper is as follows: Sect. 2 summarizes the observations and discusses the photometric and kinematic reductions. Section 3 is a morphological study based on contrast-enhanced and color index maps from the optical and near-IR images. Morphological interpretation is complemented with color, surface brightness and geometric (radial ϵ, μ, PA and a_4/a) profiles estimated by ellipse fitting to each component galaxy. A similar analysis applied to the archived (V/R and H-band) HST images for NGC 5953 is also presented. From the Fabry-Perot observations, the [N II] velocity fields, rotation curves and association of morphological with kinematic features are also presented. Section 4 is a discussion of the morphological, photometric and kinematic results followed by matching the observed morphology with the one predicted by a simulation atlas of tidal features in galaxies (Howard et al. 1993). A tentative geometry of the encounter is commented from the point of view of an interaction-AGN connection. Finally, a brief outline of the conclusions is presented in Sect. 5.

2. Observations and data reduction

NGC 5953/54 observations were obtained at the Observatorio Astronómico Nacional at San Pedro Mártir B. C. México (OAN/SPM) and are detailed in Table 1. The *BVRI* Johnson-Cousins photometry and narrow-band Hα photometry were obtained at the 1.5-m telescope in 1999 and 2001, respectively, using a Site CCD, a set of Johnson-Cousins B, V, R, I and a set of redshifted Hα filters. The near-IR JK photometry was obtained with the NIR Camera/Spectrograph CAMILA (Cruz-González et al. 1994) on the 2.1-m telescope. Finally, the interferometric [N II] observations were obtained in 1998 with

the scanning Fabry-Perot interferometer PUMA (Rosado et al. 1995) also at the 2.1-m telescope.

2.1. Optical photometry

A hybrid procedure to obtain galaxy photometry implemented by Hernández-Toledo & Puerari (2001) for both the optical and near-IR observations, developed within the standard IRAF[1] environment, is followed. Detailed and updated reduction procedures can also be found in Franco-Balderas et al. (2003).

In order to calibrate the optical images, PG 1633 and PG 1657 Landolt standard star fields (Landolt 1992) were observed during each night. At least five measurements of standard fields were made in a range of air masses for each filter. Once the principal extinction coefficients in B, V, R and I were estimated, the color terms and zero points were calculated according to standard transformation equations. For the narrow-band images, standard stars from the spectrophotometric list by Oke (1983) were observed. However, observing conditions were not photometric and the Hα images were used mainly for morphological purposes.

2.2. Near-IR photometry

Near-IR observations were obtained using a HgCdTe array of 256×256 pixels camera with 0.85″/pix plate scale and a field of view of $3.6' \times 3.6'$. Since the sky in the near-IR fluctuates considerably and is about 10^4 times brighter than the faint outskirts of the target galaxies, we had to achieve both good flat fielding and sky subtraction. We used total integration times of ∼10−12 min for J and 15 min for K-band. A list of standard stars by Hunt et al. (1998) was observed in order to calibrate the near-IR observations. Each standard star was measured on four different positions on the array and repeated at least three times each night. All the photometric observations were combined to determine zero-point offsets. Principal extinction coefficients were taken from Carrasco et al. (1991).

An estimate of the errors in the optical and near-IR photometry involves two steps: 1) the procedures to obtain instrumental magnitudes and 2) the transformation to the standard system. Total typical uncertainties are ∼0.08−0.12 mag in B, V, R, I and 0.25 in J and K-bands. The near-IR errors are conservative since no color terms were estimated from our observations. A comparison of the observed total *BVRI* magnitudes of the standard stars against those reported in Landolt (1992) show no significant deviation in any band. A similar comparison for the estimated near-IR magnitudes of the standard stars against those reported in Hunt 1998, show a $\sigma_{\rm resid} \sim 0.25$ mag, suggesting accordingly that color-term factors have not been properly taken into account.

[1] The IRAF package is written and supported by the IRAF programming group at the National Optical Astronomy Observatories (NOAO) in Tucson, Arizona. NOAO is operated by the Association of Universities for Research in Astronomy (AURA), Inc. under cooperative agreement with the National Science Foundation (NSF).

2.3. Fabry-Perot interferometry

Fabry-Perot observations of NGC 5953/54 were done at the f/7.5 Cassegrain focus of the 2.1-m (OAN-SPM) telescope with the scanning Fabry-Perot interferometer PUMA (Rosado et al. 1995). A 256×256 sector of a 1024×1024 Tek CCD detector was used with a pixel size of 0.59 arcsec. The redshifted [N II] emission was tuned by means of an interference filter centered at 6650 Å and a *FWHM* of ∼50 Å. PUMA has a free spectral range of ∼20 Å (∼915 km s^{-1} velocity range) and a sampling spectral resolution of ∼0.4 Å (19.0 km s^{-1}) at $\lambda = 6563$ Å achievable by scanning the interferometer free spectral range in 48 adjacent channels. A complete object cube of 48 min (60 s/channel) and a subsequent He (λ6676.15 Å) calibration cube were obtained.

Reduction and analysis of the data have been done using the ADHOCw[2] software. Removal of cosmic rays, bias and flat-field corrections were applied, night sky continuum and OH sky lines were subtracted and a spectral Gaussian smoothing (σ = 38 km s^{-1}) was also applied. Three spatial Gaussian smoothings (σ = 1.18, 1.77, 2.36 arcsec) were carried out on this resulting cube in order to get enough signal-to-noise ratio in the outer parts of each galaxy. The velocity maps were obtained by adjusting a Gaussian to the [N II] profile at each pixel and by fixing the wavelength origin for each pixel using the He lamp calibration cube, yielding $\sigma \sim 5$ km s^{-1} as representative uncertainties in velocities (Rosado et al. 2001). A variable-resolution radial velocity map was then built from these cubes using high resolution (less spatially-smoothed pixels) for regions with originally higher signal-to-noise ratio. Because the etalon free spectral range is larger than the range of velocities present in NGC 5953/NGC 5954, the major ambiguity in the [N II] velocities is for regions of low signal to noise (s/n) ratio. In order to detect any emission from the assumed early-type component as neatly as possible, we decided not to study this pair in the Hα light, since some stellar Hα absorption could contaminate the nebular emission. Note however, that due to the shape of the filter transmission profile, some Hα is also transmitted. The blocking filter attenuates the Hα/[N II] ratio depending on velocity, with the result that the attenuated Hα is weak compared to [N II].

2.4. Profile extraction

The reduced and calibrated near-IR and optical images are treated in the same way to extract the profiles. The images taken through different filters were aligned using foreground stars common in the frames and then matched in resolution as much as possible. We avoided using the center of the galaxies, as the morphology might be different in different passbands due to dust obscuration or interaction effects. After editing foreground stars and other inhomogeneities in each band, we ran the IRAF task ELLIPSE in free-parameter mode to the I, J and K-band frames to estimate the outer isophote parameters and transferred these parameters to all the images, thus

[2] The ADHOCw reduction package is available at `http://www-obs.cnrs-mrs.fr/ADHOC/`

making sure that further analysis was done on the same area for the different passbands.

The ELLIPSE task in STSDAS was used to perform surface photometry. This task assumes that the isophotes of a galaxy can be represented by ellipses. A description of these procedures can be found in Hernández-Toledo & Puerari (2001) and Franco-Balderas et al. (2003).

Here we remind the reader that the most dominant mode that carries information about the isophote shapes is the fourth-order cosine term, and that we have adopted its amplitude a_4/a as:

$$\frac{a_4}{a} = \frac{\sqrt{1-\epsilon}B_4}{a|\frac{\mathrm{d}I}{\mathrm{d}a}|}.$$

For a detailed discussion see Milvang-Jensen & Jørgensen (1999). Recall that a_4/a is positive for disky isophotes and negative for boxy isophotes.

We describe the orientation of each galaxy in the plane of the sky by fitting ellipses to the faintest isophotes with enough (s/n) ratio to distinguish it from both the noise level and the light contamination from a neighbor galaxy. For NGC 5953/54, the small projected separation made it necessary to create a mask around each galaxy through FIXPIX and TEXTMASK routines in IRAF. The mask was such that the ellipse fitting algorithm recognized a $w = 0$ weight within the masked region and $w = 1$ outside it. That allowed us to fit ellipses through the region of interest, reaching regions farther out compared to non-masked estimates and avoiding biased estimates due to light contamination.

3. Results

3.1. Geometric, surface brightness and color profiles

The radial behavior of the geometric profile parameters (ellipticity ϵ, position angle PA and the fourth-order cosine term of the Fourier expansion a_4/a) are presented in Fig. 1. Note that these results are obtained after a run with ELLIPSE in free parameter mode and considering a mask (one at at time) at the position of each component galaxy.

Indeed a better representation of the geometric parameters is found if an appropriate mask for each component galaxy is considered. For NGC 5953 (KPG 468A), the geometric profiles outline three regions: 1) The central and circumnuclear region ($0'' \leq a \leq 12''$) suggesting the presence of rich structure that appears intrinsically more circular than the rest of the galaxy, 2) an intermediate region ($12'' \leq a \leq 35''$) where hints of a disky structure are detected from the a_4/a profile (see also the disk observed from *B* to *K* bands in the surface brightness profiles in next section) and 3) an external region ($a \geq 35''$) suggesting, in addition to the disky structure, the presence of an external feature (an envelope?). For NGC 5954 (KPG 468B) three regions can be outlined: 1) The nuclear and circumnuclear region ($0'' \leq a \leq 20''$) that is complex in structure and is intrinsically oval in shape, 2) an intermediate region ($20'' \leq a \leq 40''$) also showing evidence of complex structure, and 3) the external region ($a \geq 40''$) where the a_4/a profile detects the presence of an external structure (an envelope?).

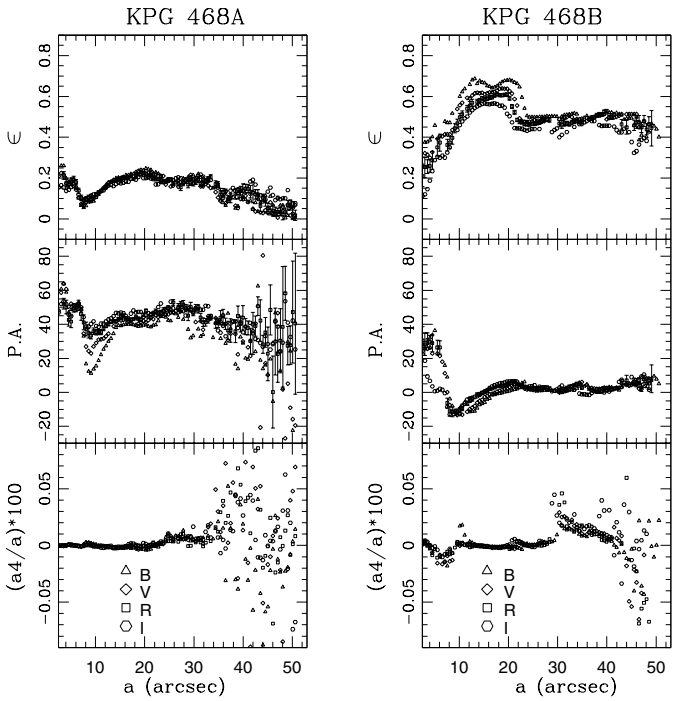

Fig. 1. NGC 5953/54: Geometric profiles after ellipse fitting in free parameter mode and masking of the galaxies.

From Fig. 1, the average representative geometric parameters are $\epsilon = 0.18 \pm 0.1$, PA $= 45 \pm 10$ for NGC 5953 and $\epsilon = 0.48 \pm 0.1$, PA $= 2 \pm 7$ for NGC 5954. These were taken as the input parameters to estimate the surface brightness and color profiles after running ELLIPSE in fixed parameter mode, where in addition, a mask was used to eliminate contamination from the neighbor galaxy. We preferred this method of fixed parameters for each radius because it enables us to compare the profiles measured in the different passbands. The resulting luminosity and color profiles are shown in Fig. 2.

Using a mask for each component galaxy means that a reestimate of a representative sky value is needed. This critically controls the behavior of the profiles in the most external regions. Thus, we emphasize that the behavior of the profiles within the first 40″ is more reliable.

For NGC 5953, the color profiles show evidence of a blue dip also in the first 10″, suggesting that the internal structure is bluer than the rest of the galaxy. The shape of all the surface brightness profiles is indicating the presence of an underlying disk visible in the external region. For comparison, notice that the major axis *V*-band surface brightness profile for NGC 5953 published by Reshetnikov (1993) tends to rise after 30″, probably reflecting the need of an extra image processing to eliminate light contamination from the companion galaxy. NGC 5954 is a blue galaxy as evidenced from the color profiles. Although the optical color profiles tend to be flat, the optical-to-near-IR colors resemble those of late-type spirals. The major axis *V*-band surface brightness profile for NGC 5954 published by Reshetnikov (1993) is more similar to our *V*-band profile within 30″. However, the presence of a plateau after 30″ in his profile is also noticeable, suggesting possible light contamination from the neighbor galaxy.

Table 2. Observed magnitudes and color indices.

NGC	*B*	*V*	*R*	*I*	*J*	*K*	*B* − *V*	*B* − *R*	*B* − *I*
B − *J*	*B* − *K*	*J* − *K*							
NGC 5953	13.29	12.46	11.84	11.16	10.27	9.24	0.82	1.45	2.12
3.01	4.04	1.03							
	13.18(Ra)	12.06 ±0.1(Re)		11.46(Hu)	10.54(Hu)	9.53(Hu)			
NGC 5954	13.56	12.91	12.42	11.81	10.98	9.97	0.65	1.15	1.76
2.59	3.60	1.01							
	13.65(Ra)	12.67 ±0.1(Re)							
Normal spirals							0.78(dJ)		1.81(dJ)
	3.65(dJ)								

Re = Reshetnikov (1993).
Ra = Rampazzo et al. (1995).
Hu = Hunt et al. (1999).
dJ = de Jong (1996).

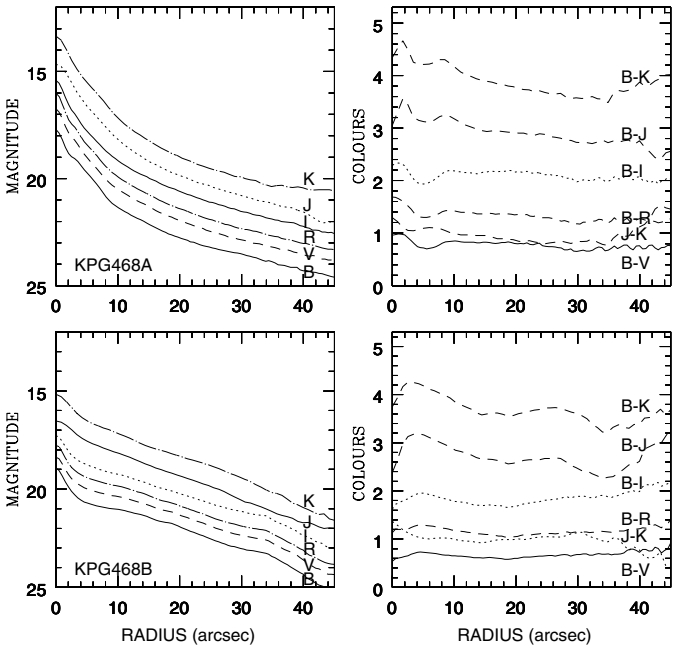

Fig. 2. Surface brightness and color profiles (masked companion).

3.2. Integrated magnitudes and colors

Total magnitudes in the optical and near-IR bands can be calculated by analytically extrapolating a fit disk beyond the outermost isophote to infinite. However, disk fitting is notoriously fraught with uncertainty (cf. Knapen & van der Kruit 1991). Alternatively, we estimated total magnitudes from polygonal apertures properly chosen within the POLYPHOT task in IRAF. In this method polygonal apertures can be interactively delineated according to the global shape of the galaxies and their degree of interaction. Note that foreground stars within the apertures were removed interactively.

The estimated total magnitudes and colors of the component galaxies in NGC 5953/54 are presented in Table 2. Column 1 gives the identification in Karachentsev Catalogue, Cols. 2 to 7 give the observed total magnitudes in *B*, *V*, *R*, *I*, *J* and *K* bands and Cols. 8 to 13 give the observed $(B - V)$, $(B - R)$, $(B - I)$, $(B - J)$, $(B - K)$ and $(J - K)$ color indices. Total typical uncertainties in our photometry are 0.1, 0.1, 0.13 and 0.14 for *B*, *V*, *R* and *I* and ∼0.25 in *J* and *K* bands, respectively. Table 2 also includes the estimates from other authors, when available.

Reshetnikov (1993) reports total *V*-magnitudes for each galaxy. However if the rise in the NGC 5953/54 major axis surface brightness profiles (Figs. 2 and 3 in his paper) is due to light contamination from the companion galaxy, his total *V* magnitudes are expected to be brighter than our values. On the contrary, Rampazzo et al. (1995) report total blue magnitudes $B_{\rm T}^{\circ} = 13.18$ and 13.65 for NGC 5953 and NGC 5954 respectively, in agreement within the errors, with our *B*-band estimates.

For the near-IR observations, the Catalog of Infrared Observations by Gezari et al. (1993) reports $J = 11.33$ and $K = 10.34$ mag for NGC 5953 and $J = 13.08$ and $K = 10.29$ mag for NGC 5954. The data comes from Joseph et al. (1982) and Cutri (1990) both from small aperture (8−12″) photoelectric near-IR photometry. An estimation of our magnitudes at a 10″ aperture indicates $J = 11.19$ and $K = 10.17$ for NGC 5953, and $J = 12.90$ and $K = 10.59$ mag for NGC 5954, basically in agreement with those values within the estimated errors. More recent *I*, *J* and *K*-band magnitudes (30″ aperture) for NGC 5953 by Hunt et al. (1999) are also in agreement with our estimates within errors.

Table 2 also shows a relative comparison of the observed colors of NGC 5953/54 by taking as a reference, the integrated mean colors for normal spirals obtained from de Jong (1996). Notice that the colors of NGC 5954 are similar to those of

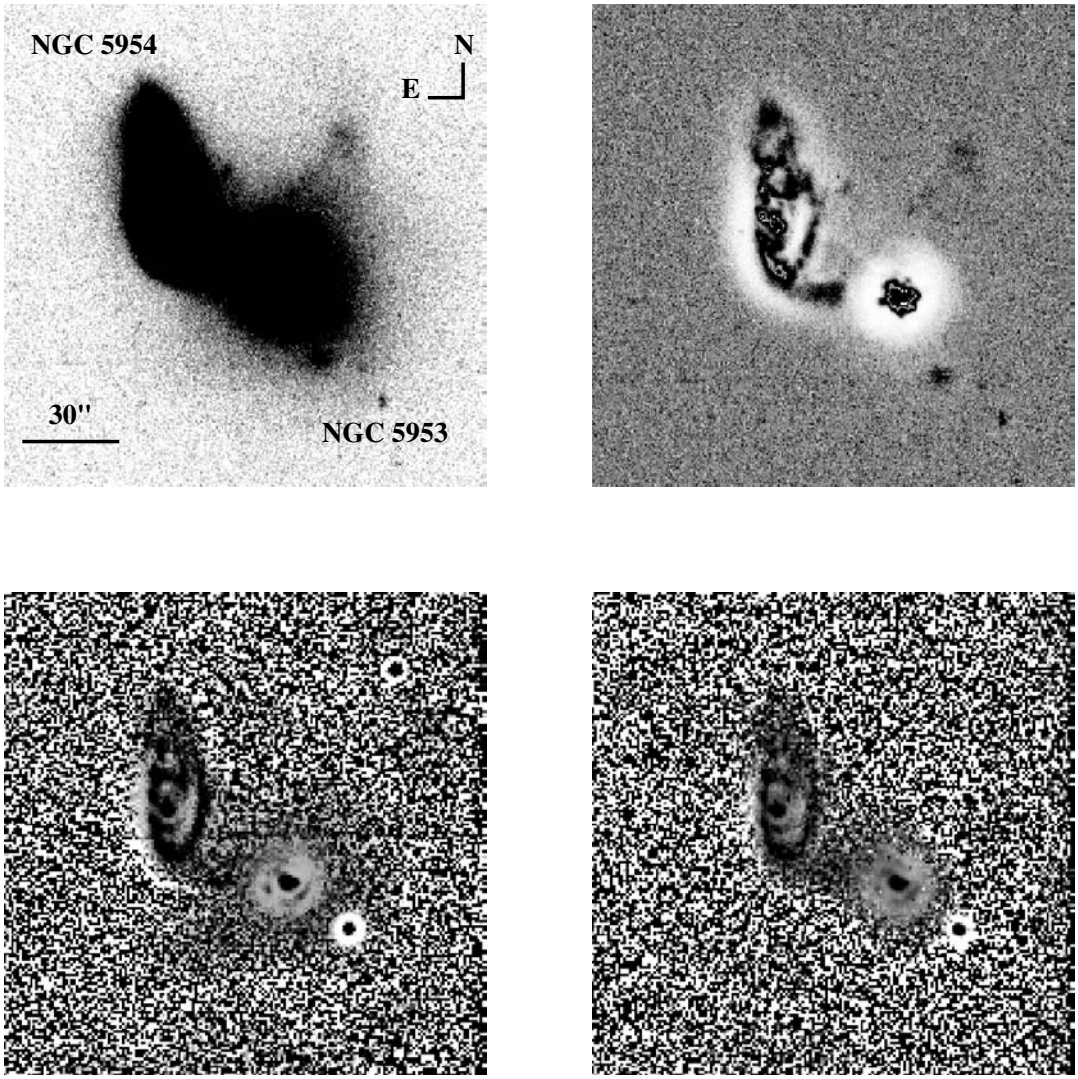

Fig. 3. *Top left*: full intensity *B*-band image. *Top right*: *B*-band contrast-enhanced image. *Bottom left*: *J*-band contrast-enhanced image. *Bottom right*: *K*-band contrast-enhanced image.

normal spiral colors while those of NGC 5953 are redder in general. Furthermore, the optical-to-near-IR colors of NGC 5953 tend to be redder than those expected for normal spirals. A similar result was reported by Hunt et al. (1999) from near-IR studies in samples of Seyfert galaxies. A more careful analysis including this topic is reserved for a forthcoming paper.

3.3. Morphology

Kinematic data from the literature yields a systemic velocity (corrected for solar motion) for NGC 5953/54 as a whole of 1921 km s^{-1} implying a distance D = 26.7 Mpc (H_o = 75 km s^{-1} Mpc^{-1}). From this and for the sake of the following discussion, a scale in our images of 1″ = 0.13 kpc and a projected separation of ∼5.8 kpc are assumed. To discuss the optical morphology and its relationship to the global photometric properties, we start by showing a series of images, all of the same size (2.53′ × 2.53′). The upper left panel in Fig. 3 shows a full intensity gray-scale *B*-band image of NGC 5953/54, while the rest of the panels show contrast-enhanced images in *B*, *J*, and *K*-band respectively. The contrast-enhancing techniques (Sofue 1993), allow the subtraction of the diffuse background in a convenient way to discuss the presence of extinguished dust and luminous internal regions.

In addition, the upper left panel in Fig. 4 shows a [N II] image from the Fabry-Perot cube with composite resolution. Regions of high signal to noise ratio (s/n) are displayed at full spatial resolution (∼1.5″) while regions of moderate or low (s/n) were smoothed with Gaussians of several pixel *FWHM*. The upper right panel shows a continuum-subtracted Hα image displayed at full intensity level. The lower left panel shows a contrast-enhanced Hα image.

3.3.1. NGC 5953

From the full intensity *B*-band image, NGC 5953/54 seems to be a slightly overlapping pair. A considerable confusion about the morphological type of NGC 5953 can be noticed in the literature (see Table 3).

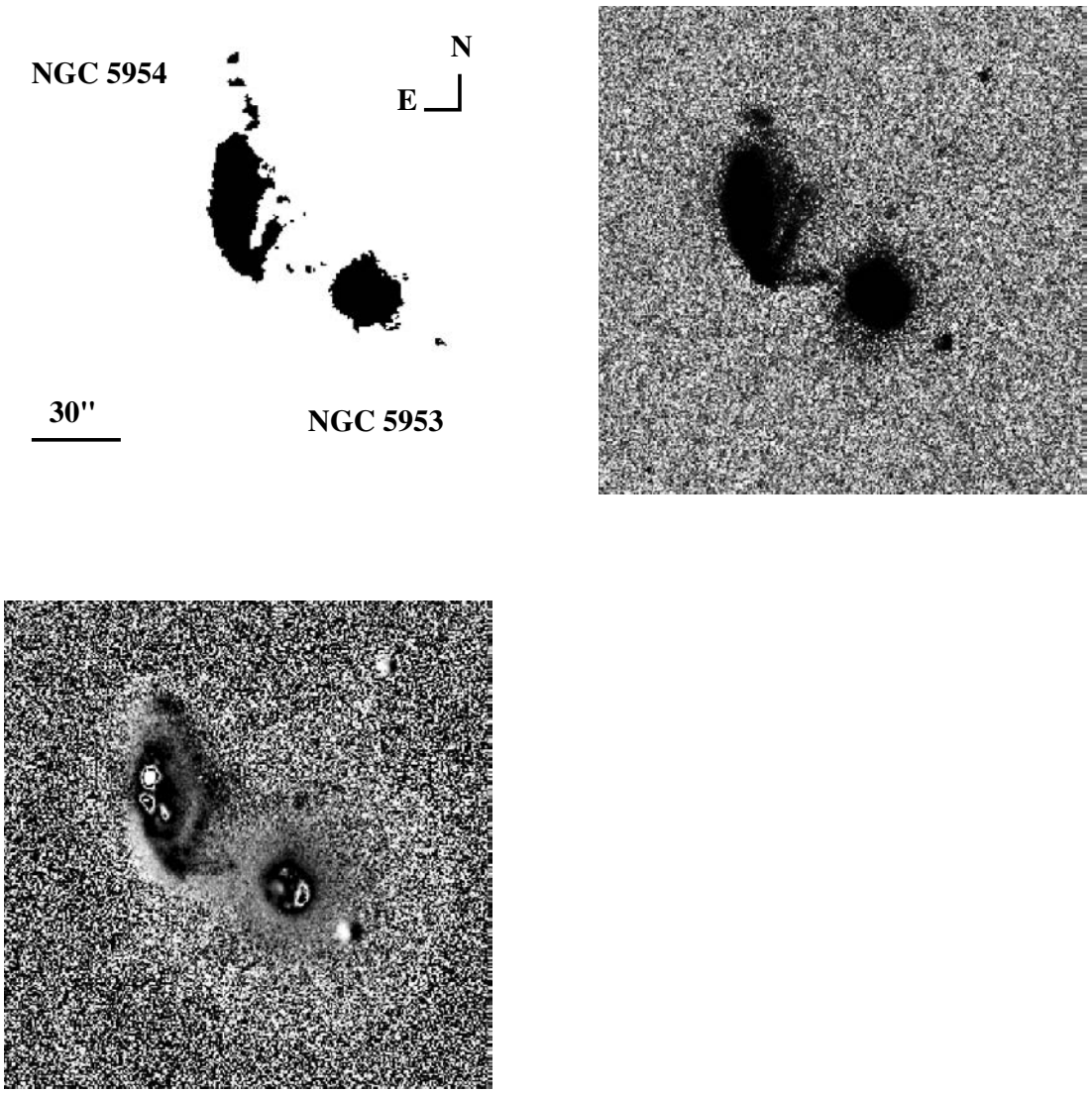

Fig. 4. *Top left*: composite resolution [N II] image. *Top right*: continuum-subtracted Hα image. *Bottom left*: Hα contrast-enhanced image.

Table 3. General data for NGC 5953/54.

NGC number	NGC 5953	NGC 5954	References
Name(s)	UGC 9903	UGC 9904	
	KPG 468A	KPG 468B	
	MRK 9031A	MRK 9031B	
Morphology	S0-a	SBc	LEDA
	SAa:pec;LINER;Sy2	SAB(rs)cd:pec Sy2	NED
	.SA.1*P	.SXT6*P	RC3
	Sa	Scd	Reshetnikov (1993)
	S0	SAB(rs)	Rampazzo et al. (1995)
	S0	Sc?	Nilson (1973)
	S0	Sc	Karachentsev (1987)
M_B	−18.89	−20.26	LEDA
Projected distance	45 ± 2″ (5.8 kpc)	45 ± 2″ (5.8 kpc)	

The *V*-band photometric study by Reshetnikov (1993) describes NGC 5953 as a galaxy with a relatively bright and compact bulge, with an exponential disk brighter and more compact with respect to the average disks of normal galaxies of the same morphological type (Sa). The *B*-band photometric study by Rampazzo et al. (1995), suggests that NGC 5953 is either an S0 galaxy with evidence of knots near the center and a lack of spiral structure, or that it is an early-type galaxy where the gas component has been acquired from the spiral member in the interaction.

A linear feature (plume) is clearly seen at the NE from NGC 5953 in all the broad-band optical images. This is probably the stellar counter-part of the HI plume reported in the HI 21 cm study by Chengalur et al. (1994). In addition, the linear feature is seen apparently ending in a clump-like region. The optical clump (if real) may be the result of self-gravity causing clumping of the emerging material. Numerical simulations (Barnes & Hernquist 1992) show that self-gravity in tidal debris leads to the formation of gas-rich stellar knots. Such knots have some observational support (cf. Mirabel et al. 1991; Hibbard et al. 1994).

In the previous section, the geometric and surface brightness profiles suggested the presence of a blue inner structure and an underlying disk for NGC 5953 that now can be identified with a star-forming circumnuclear region and a structureless external disk, respectively. The Hα contrast-enhanced image shows the presence of recent star formation in a circumnuclear ring, ∼11.6″ (∼1.5 kpc) in diameter. According to González-Delgado & Pérez (1996), all their measured H II regions in NGC 5953 have luminosities larger than 10^{39} erg s^{-1}, the limiting luminosity used by Kennicutt (1983) to define a supergiant H II region.

In addition, the continuum-subtracted Hα and composite resolution [N II] images (cf. Fig. 4) show evidence of a broad tide-counter-tide feature to the north and south. The fan-like nature of these tides suggests that NGC 5953 may have suffered a close retrograde encounter with NGC 5954. Since tidal disturbances are two-sided, we suggest that the linear feature (plume) NW of NGC 5953 may be an extension of the bridge apparently emerging from NGC 5954 and that seems to connect the two galaxies.

The *J* and *K*-band contrast-enhanced images also show traces of the circumnuclear region in NGC 5953. Thus this feature is stellar and shows up also in the ionized gas (Hα imaging). Notice a small star at ∼3″ (0.387 kpc) from the center of NGC 5953, more easily seen in the *J* and *K*-band images, but present in all the observed bands.

3.3.2. NGC 5954

The *B*-band contrast-enhanced image of NGC 5954 shows an intricate morphology. Among the most definite features, we can mention: 1) Strong star-forming knots all along its face, with high surface brightness regions seen preferentially to the east (far side with respect to NGC 5953). 2) A prominent arm, extending northwards and apparently emerging at the base of the bridge. 3) Traces of a faint inner arm, eastward of the prominent arm, and apparently emerging near from the circumnuclear region. 4) A set of filaments differing in curvature from one another and giving the appearance of bubble-like features to the north and northeast. A clump is noticed at the top of the northmost bubble. 5) An inter-arm region that runs along the inside edge of the prominent arm and between this and the faint inner arm, and 6) a bridge apparently connecting NGC 5954 with NGC 5953, visible as a broad feature in the optical and near-IR bands and as a narrow filamentary feature in the [N II] and Hα bands.

The narrow-band Hα images confirm the presence of prominent star-forming regions all along the disk and of a circumnuclear (though somewhat elongated along the apparent major axis of NGC 5954) star-forming region. The apparent surface brightness asymmetry in the optical towards the eastern side of NGC 5954 vanishes in the near-IR where both arms appear almost equally bright, showing different curvature and with the inner-most arm running to the north and ending into a clump. If explained as an inclination effect, this may be telling us that the eastern side is the near side. González-Delgado & Pérez (1996) suggest that 85% of the measured H II regions in NGC 5954 are super-giant H II regions with luminosities greater than 10^{39} erg s^{-1}. Our composite [N II] image, also shows a long prominent extension running to the north and curving toward the north-east at its northern end. This extension is seen bordering the western side of the bubble-like features and is interpreted as a tidal feature.

The contrast-enhanced *J* and *K*-band images also show two almost equally bright arms with different curvatures. The inner-most emerges from a now well-defined oval circumnuclear region, as previously inferred from the geometric profiles. NGC 5954 reveals itself more clearly as an eye-shaped galaxy in the near-IR bands, where the double parallel arm structure may be interpreted as a tidal tail and a streaming arm on the side close to the companion. Similar cases in other interacting pairs have been previously reported (cf. Kaufman et al. 1999). Definite traces of the filaments to the north are also visible. A photometric center can be well defined and, similarly to NGC 5953, definite traces of the circumnuclear region can also be seen. On the northeast side of NGC 5954 there are two bubble-like features clearly visible in the *B* to *I*-band images, but weakly visible in the *J*, *K*, Hα and [N II] images. Our Fabry-Perot observations detect the presence of double profiles at the base of the southern bubble-like feature.

Due to the presence of a circumnuclear oval and the inner arm, its is difficult to make a clean estimate of the stellar arm-interarm contrast. By taking as a reference the inner edge of the main arm, we obtain an average arm-interarm contrast from 0.6 to 0.8 mag from *B* to *J*-band, consistent with normal spiral arms (Regan & Elmegreen 1997). If we make the same estimate by taking as a reference the sky background on the western side of the main arm, then the average arm contrast rises from 1.7 to 2.0 mag from *B* to *J*-band images, respectively. Galaxy encounter simulations (Elmegreen et al. 1995) predict a large stellar arm-interarm contrast for tidal arms at certain stages in a prograde encounter. The observed values for the northwestern arm of NGC 5954 are marginally consistent (within the estimated errors) to those predicted for a tidal arm.

3.4. Color maps

In order to make the color maps, all the images through different filters were aligned using foreground stars common in the frames and then matched in resolution as closely as possible. The highest contrast (at the same resolution) is obtained with the optical $(B-I)$ color map, whereas the optical to near-IR color maps implied a matching that slightly degraded the quality of the $(B-J)$ and $(B-K)$ color maps. At the edge of these maps noise dominates, but closer to the nucleus the colors are more reliable. We checked that the color residuals of field stars do cancel out in the color maps. Figure 5 shows our $(B-V)$, $(B-I)$, $(B-J)$, and $(B-K)$ color index maps.

A problem with the interpretation of the color maps is the contamination from emission lines within the broad bands (cf. Kotilainen & Ward 1997; hereafter KW97). If the B, I, J, and K filters are dominated by the continuum emission, then the $(B-I)$, $(B-J)$, and $(B-K)$ color-index maps are more free from emission lines and allow us to observe the features dominated by the continuum emission. Whereas the I, J, and K-band images show a smoother distribution mainly from a population of more evolved stars, the B and V-band images reveal the presence of absorbing dust, H II regions and young stars. Thus, given the filter widths, the $(B-V)$ color map is useful to trace the spatial distribution of the star formation on time scales of $\sim 10^9$ years, whereas we would expect to detect clumpy, ring-like or elongated blue or red structures with a maximum of contrast in the $(B-I)$, $(B-J)$, and $(B-K)$ color maps.

3.4.1. NGC 5953

There has been increasing evidence, specially for Seyfert galaxies (KW97) that in Seyfert 2's optically thick material, in the form of a thick disk or a dusty torus, blocks our direct viewing of the compact nucleus and the broad line region (BLR), and collimates the ionizing photons along the minor axis of the torus into two oppositely directed cones. Most of the emphasis in studies of the nuclear regions of Seyferts has been put on the emission line properties (cf. integral field spectroscopy and emission line imaging). However, although the nuclear torus is expected to be too small to be resolved, its effect on the circumnuclear region in the form of a flattened dust distribution may be detectable. Because this material is expected to be redder than the surrounding stellar population, the geometry of the obscuring region should be apparent in color-index maps.

Notice that all our color maps show an inner reddened arc E-N-W surrounding the nucleus of the Seyfert 2 NGC 5953. This may be consistent with the expectations in (KW97). Besides the clear trace of the circumnuclear region, $(B-V \sim 0.55)$, the $(B-V)$ map also shows a central faint blue narrow elongation at PA $\sim 45°$. This structure has a similar orientation to the high ionization region northeast from the nucleus of NGC 5953 at PA $\sim 50°$, reported by Yoshida (1993), and similarly, to the northeast linear structure seen in the [OII]/Hα excitation map at PA $\sim 44°$ reported by González-Delgado & Pérez (1996). Surprisingly, our Fabry-Perot observations detect double profiles at the same PA but at the opposite (southwestern) side. Other studies of continuum color index maps have revealed blue morphological features coincident with the high-excitation gas in the extended narrow line region (ENLR) (cf. Mulchaey et al. 1996; KW97).

A more external N-E-S ($\geq 15''$) region with higher reddened colors ($B-V \sim 1$ mag) is also visible in the optical-to-near-IR maps. This could be reflecting the presence of dust associated with the gas distribution at that position in NGC 5953. Chengalur et al. (1994) reported considerably more HI on the side nearer to NGC 5954 than away from it. From the color maps diffuse traces of an underlying structure (maybe the disk) are detectable for the external region ($\geq 15''$) of NGC 5953.

3.4.2. NGC 5954

Similarly to NGC 5953, a strong circumnuclear region ($B-V \sim 0.55$) can be traced for NGC 5954. This galaxy is suffering a global episode of star formation as judged from the observed color maps. Notice that the southern-most region of the disk and the adjacent bridge region share basically the same colors ($B-V$ between 0.45 and 0.55 mag), suggesting that the bridge could be originated in NGC 5954 as a by-product of the interaction. The filaments delineating the northern bubble-like structure are visible in the color maps as a "Y" feature to the north of the circumnuclear region in all the color maps (but see the $(B-J)$ and $(B-K)$ color maps). This "Y" feature is one of the bluest regions ($B-V \sim 0.3$ mag) in this galaxy. The clump at the top of the bubble-like feature is also blue ($B-V \sim 0.4$ mag). The crowding of the orbits and the subsequent compressing of the gas in this region is probably causing an enhancement of star formation. Interestingly, it is at the western border of the "Y" feature where our Fabry-Perot observations detected the presence of double profiles. The inter-arm region (seen here between the circumnuclear region and the northwest arm) can be recognized as a red linear ($B-V \sim 0.8$ mag) feature running parallel to the northwest arm. We notice that the $(J-K)$ color map (not shown here), also shows clear traces of the circumnuclear region and the "Y" feature associated with the northern-most bubble, reinforcing their stellar nature.

3.5. HST images and surface brightness profiles of NGC 5953

To complement our discussion on the surface photometry and morphology of the Seyfert 2 NGC 5953, we have retrieved and analyzed the available HST images observed with the WFPC2 F606W filter and the H-band (1.6 μm) F160W filter. The F606W filter includes both the standard WFPC2 V and R bands and has a mean wavelength of 5940 Å. The exposure time was 500 s. The plate scale is 0.046″/pix and a field of view of $37'' \times 37''$. The F160W filter in the Near-Infrared Camera and Multi-Object Spectrometer (NICMOS) give a field of view $19.2'' \times 19.2''$ and a pixel scale of 0.075″/pix. The exposure time at H-band was 320 s. As these images belong to snapshot survey programs, the exposure times were relatively short.

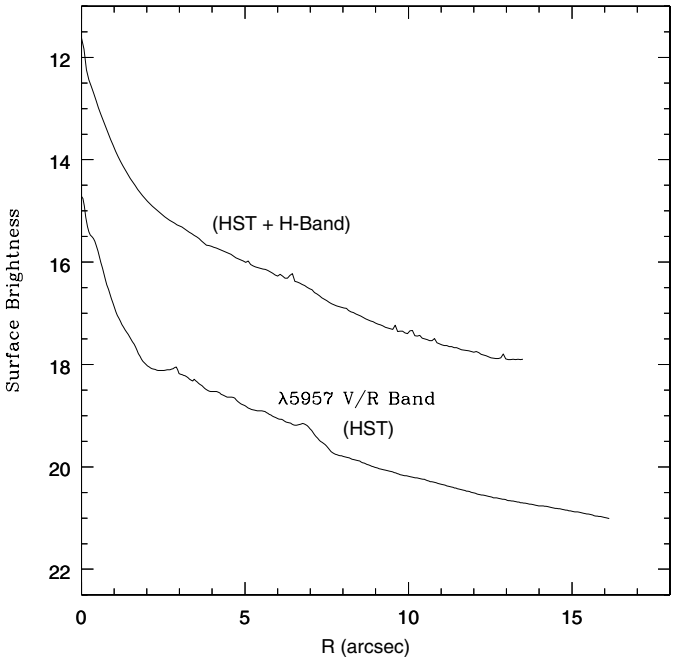

Fig. 6. The HST (V/R) and H-band surface brightness profiles of NGC 5953.

Data reduction of HST images begins with the standard pipe-line processing performed at the STScI. Cosmic-ray removal made use of standard routines in IRAF, taking care of not to affect any real features. In addition, some extended hits, tightly confined to a few pixels were also removed. A number of bad pixels in the NICMOS array were edited or masked from the images. We used the ELLIPSE task in STSDAS to perform surface photometry on these images. The V/R and H-band calibrated magnitudes were computed by using the photometric keywords provided in the image header after converting observed counts to the Vega magnitude system. We did not try to subtract the sky background from these images because the galaxies are extended more than the physical size of the chips. Figure 6 shows the estimated HST (V/R) and H-band surface brightness profiles of NGC 5953.

A detailed discussion of the deconvoluted HST profiles, including a simultaneous fitting to the [N II] rotation curves of NGC 5953/54 (maximun disk solution) is reserved for a forthcoming paper.

The upper panel in Fig. 7 shows our contrast-enhanced B-band image of NGC 5953 and a zoom of its central region as viewed from the WFPC2 λ5957-band in HST. Similarly, the lower panel shows a contrast-enhanced J-band image and a zoom of its central region, as viewed from the NICMOS H-band from HST. Notice that contrast-enhancing was also applied to both V/R and H-band images from HST.

The HST's order-of-magnitude improvement in spatial resolution adds new elements to the current morphological classification systems (cf. Malkan et al. 1998) and may well have shown us the tip of the iceberg for new/extended classification schemes. Thus for the sake of clarity, we only have attempted here to note features that are clearly evident to everyone who has viewed the images. The more difficult task is in interpreting the significance of these features, but our interpretation will be reserved for a forthcoming paper.

NGC 5953 shows significant deviations from smooth isophotes caused either by localized excess of emission (star clusters and H II regions) or deficits (dust absorption). In contrast to "grand design" spirals with a few very long arms, the disk of NGC 5953 has dozens to hundreds of barely resolved patches wrapped in tight spirals. Our Hα imaging and other previous studies (cf. González-Delgado & Pérez 1996) clearly showed a circumnuclear ring. The resolution of rings into knots is becoming a frequent result as higher resolution is attained. However, previous attempts can be dated back to Sérsic & Pastoriza (1965) for a set of galaxies with nuclear hot spots.

In spite of the apparently regular spiral pattern, a careful look at the HST images show clear indications of disturbances, leaving a pattern far from being symmetric either locally (see the irregularity of pitch angles at the eastern arms) or globally (see the northeast-southwest asymmetry giving the appearance of an inclined oval disk). These images may be showing evidence either of dust lanes or irregular absorption patches associated with the spiral arm pattern. This is consistent with the findings that the centers of Seyfert 2's are intrinsically dusty environments. This suggestion is not new. Seyfert 2's are statistically redder than Seyfert 1's at all wavelengths from the far-infrared to the X-rays, and a relatively larger fraction of their total energy output has been reprocessed by warm dust grains (cf. Edelson & Malkan 1986). Other possibility is that this local/global asymmetric irregularity may be evidence of a kind of temporary crowding/oscillation caused by the interaction process. Notice that in spite of the increase in spatial resolution and sensitivity, NGC 5953 shows no evidence of any external morphological feature except for the disk itself. The inner concentration of the spiral pattern may be revealing efficient mechanisms for angular momentum transport in NGC 5953 during the interaction. This, in complement to our broad-band results, strongly points to a special geometry of the encounter for NGC 5953, as discussed in the following sections.

The nuclear region of the Seyfert 2 NGC 5953 show no clear central point source at the HST resolution, but instead, an "s" feature revealing the presence of a probable bar. This component is ~60 pc in radius, at about the same PA as the the global major axis of the galaxy. Barnes & Hernquist (1996) modeled barred potentials and showed that they are effective in driving interstellar matter into the nucleus and fueling increased nonstellar activity there, assuming that a massive black hole is already present. See also Shlosman (1994).

3.6. Fabry-Perot velocity fields and rotation curves

3.6.1. NGC 5953 velocity field

Kinematics of NGC 5953 is presented in Fig. 8 which shows the [N II] variable spectral resolution isovelocity map overlaid on a gray-scale [N II] variable spatial resolution image.

Figure 8 shows that the [N II] emission in NGC 5953 is concentrated within the inner 12″, and that the velocity field resembles one of a non-perturbed spiral galaxy.

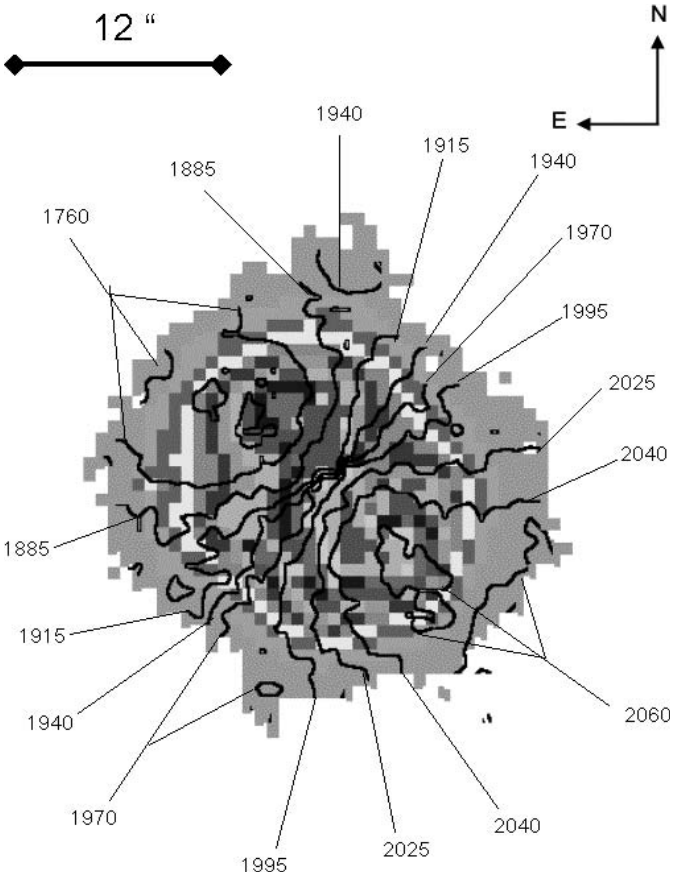

Fig. 8. [N II] isovelocity map for NGC 5953.

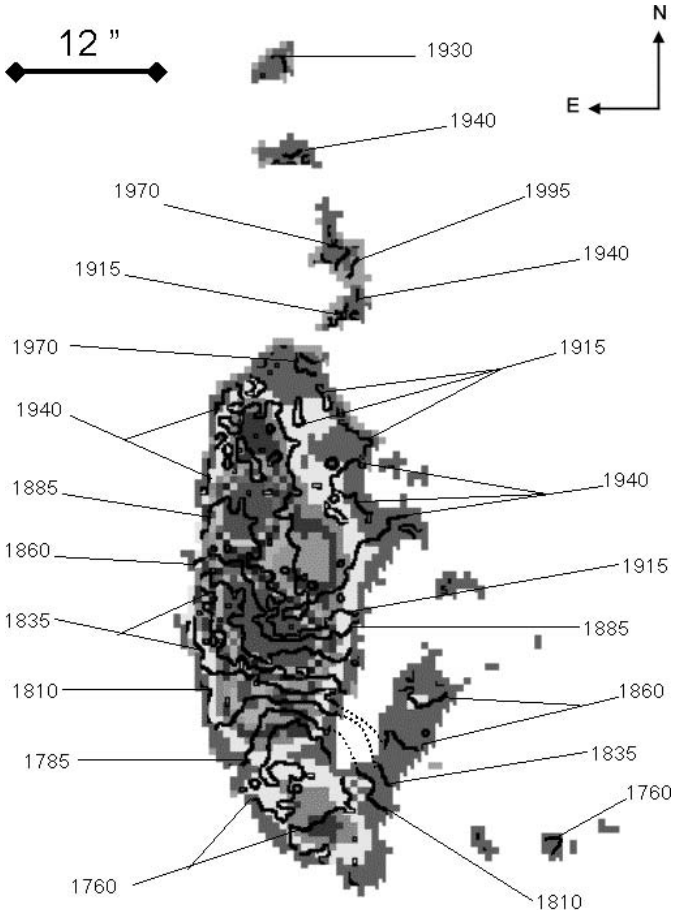

Fig. 9. [N II] isovelocity map for NGC 5954.

The kinematical minor axis is perpendicular to the apparent major axis and the velocity field is quite symmetric. On the southwest side of the galaxy, at 11″ from the center, double velocity profiles were detected. Interestingly, at the opposite side (northeast), a high ionization region has been reported by Yoshida (1993) and González-Delgado & Pérez (1996). The receding side of NGC 5953 is the south one and the approaching side is the northern one. Notice that contrary to the case of NGC 5954, in NGC 5953 we do not find any key to infer which is the near side and deduce the rotation sense. See however Sect. 4.2. From this velocity field, it is difficult to recognize any evidence of streaming or other global motions. If we adopt the HI velocity contour $v = 1970\,\mathrm{km\,s^{-1}}$ through the nucleus as representative of the kinematic minor axis, then the line of nodes of the projection perpendicular to the kinematic minor axis has a PA similar to the average value inferred from our photometry. Notice however, that from Fig. 1 the photometric major axis is changing in the inner 12″. This misalignment between the photometric and kinematic axes in the central region could be indicating an intrinsically different shape for the central disk of NGC 5953.

3.6.2. NGC 5954 velocity field

Kinematics of NGC 5954 is presented in Fig. 9 which shows the [N II] variable spectral resolution isovelocity map overlaid on a gray-scale [N II] variable spatial resolution image.

Contrary to NGC 5953, the velocity field of NGC 5954 is much more extended and quite distorted (Fig. 9). There is no symmetry between the northern side of the galaxy (receding velocities and farther in projection from the companion) and the southern one (approaching velocities and closer in projection to the companion). Assuming that the western side is the near side (see Sect. 4.2), the rotation is clockwise. Notice an inverted S-type distortion of the global velocity field. This global twisting may be caused in part by streaming motions on the tidal arms. On the northwestern side, double velocity profiles were detected at the base of the northern-most bubble seen in our optical images. Our photometry in Fig. 1 shows a clear distinction in the shape of the inner 22″ with respect to the more external region. This significant misalignment between the photometric and the global kinematic axes in the central region is confirming the intrinsically oval shape for the central disk. These differences are not unusual for interacting galaxies (Kaufman et al. 1999; Fuentes-Carrera et al. 2003). Similar discrepancies have also been found in isolated nearby spirals (Andersen & Bershady 2002).

At 28″ from the kinematical center, the galaxy shows a [N II] tail ∼30″ long, extending all the way to the north and delineating the western border of two large bubble-like features. The radial velocities of this feature range from 1922 $\mathrm{km\,s^{-1}}$ to 2001 $\mathrm{km\,s^{-1}}$. The largest observed velocities along this structure are located at 32″ from the center, almost at the

base of this feature. The southern bubble-like feature can be associated with a crowding of the iso-velocity contours at about 1940 km s^{-1}, but insufficient [N II] signal at the position of the northern bubble-like region gives no clues about its kinematics, except that on this same northwestern side, double velocity profiles were detected.

The [N II] isovelocity contours through the nuclear region are strongly curved. If we were to identify the [N II] kinematic minor axis in this region by adopting the velocity contour with $v = 1860 \pm 5$ km s^{-1}, the position of the nucleus would be displaced about 3″ with respect to the baricenter of the light in our *K*-band images. This may imply that the dynamical center could have been moved as a result of the interaction. However, notice that NGC 5954 appears somewhat lopsided in our near-IR images and that it is possible that the mass distribution may not be intrinsically centered at the nucleus.

The crowding of the isovelocity contours along the eastern side of NGC 5954 can be associated with the eastern chain of giant H II regions visible in the *B*-band and Hα images. This may be evidence of streaming motions associated with local star formation. In the bridge region, the radial velocities changing gradually from $V_{\rm rad} \sim 1780$ km s^{-1} (similar to the values in NGC 5954) to $V_{\rm rad} \sim 1880$ km s^{-1} (close to values in NGC 5953). Thus, from our [N II] Fabry-Perot observations it is not possible to infer the true kinematical association of the bridge. From this velocity field, it is difficult to say something about the kinematics of a spiral density wave probably present in NGC 5954.

3.6.3. [N II] properties

Figure 10 displays channel maps (a few channels) made from a smoothed [N II] cube overlaid on our *B*-band contrast-enhanced image in gray scale.

[N II] emission from both galaxies is present over the whole range of observed velocities. This makes it difficult to separate the [N II] contributions of each companion. The peaks of the [N II] emission are associated with the large H II regions in both galaxies. Although the [N II] emission is strongly confined in NGC 5953, it is also visible as a diffuse fan-like component to the north and south that we interpret as of tidal nature. Faint emission is detected in a region 25″ to the southwest of the galaxy with radial velocities considerably larger than those associated with the main galaxy ($V_{\rm rad} > 2240$ km s^{-1} for that region, compared to $V_{\rm rad} < 2100$ km s^{-1} for the galaxy). Even though the feature falls within the 23.5 *B*-band isophote and is detected in all the observed wavelengths, the lack of continuity in the [N II] emission in that region suggest that it is probably due to a highly reddened field star.

The [N II] tail to the north and northeast of NGC 5954 is also visible in the channel maps. A careful superposition at different surface brightness levels shows that the [N II] emission is somewhat displaced with respect to the *B*-band bridge emission, probably showing differences in motions of the stars and the gas in that region. Similar behavior is observed in (S+S) isolated galaxy pairs such as Arp 271 (Fuentes-Carrera et al. 2003). If the bridge region is associated with the southeastern arm of NGC 5954, then this mismatch could reflect the motion of the perturbation responsible for the enhanced star formation in that region. Interestingly, the spectroscopic study by Rampazzo et al. (1995) obtained along a line connecting the centers of the two galaxies, indicates that the stars and gas show similar steep rotation curves but also a striking spatial displacement. The rotation velocity deduced from the gas is ∼100 km s^{-1} higher. The striking plume to the northwest of NGC 5953, visible in the contrast-enhanced *B*-band image and also reported in the HI 21-cm study by Chengalur et al. (1994), is not detected in our [N II] interferometric study.

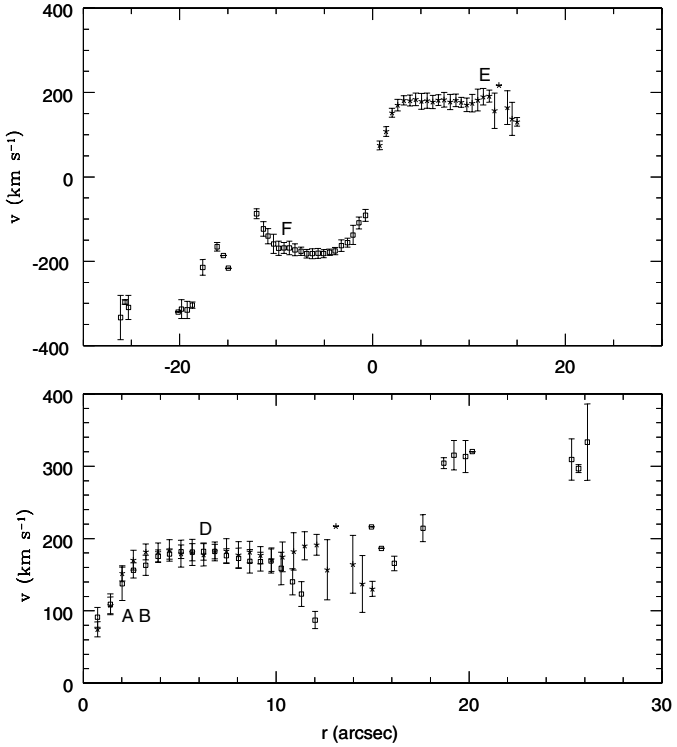

Fig. 11. [N II] rotation curve for NGC 5953.

3.6.4. NGC 5953 rotation curve

In order to compute the rotation curve, we considered those points within an angular sector of 42° on each side of a representative major axis for this galaxy. A PA of (51.5 ± 10)°, an inclination of (32.0 ± 2)°, and a systemic velocity of $V_{\rm syst} = 1962.0$ km s^{-1} were chosen, in order to obtain a symmetric curve in the inner parts of the galaxy and to minimize scatter on each side of the curve.

The resulting [N II] Fabry-Perot rotation curve for NGC 5953 (KPG 468A) is shown in the upper panel of Fig. 11. The lower panel shows the superposition of both branches of the rotation curve.

The rotation curve is rather symmetric in the inner 10″. For both sides of the galaxy, the rotation curve rises slowly out to ∼3.5″ from the center reaching a velocity of 175 km s^{-1}. It then remains flat out to ∼10″. After that point the rotation curve shows a bifurcation: the velocity begins to decrease for the approaching side (the one closer to the companion)

reaching ∼90 km s^{-1} at 12″ from the center, while at other position an increase of the curve up to ∼300 km s^{-1} at ∼20″ is observed. The strong velocity oscilation in this region may well be associated with the effective tidal impulse of the companion (see Sect. 4.1) as well as the strong influence of non-circular motions.

For the receding side (southwest side and farther from the companion), the curve remains flat up to 11″ then it increases slightly reaching 195 km s^{-1} at about 12″. However, a few external points suggest a decrease of the curve down to ∼130 km s^{-1} at ∼15″. The spectroscopic data from Reshetnikov (1993) also shows evidence for a turnover on both ends of the rotation curve.

At ∼11″, double velocity profiles appear on the southwestern part of the galaxy. In order to assign a single radial velocity (and thus a single $V_{\rm rot}$) to double profile points, we took as a first option, the velocity of the most intense component. If the intensities were similar for both components, we selected the adjacent points where there was still a significant difference in the profile intensities. For these points, the curve shows strong oscillations.

A closer association of the velocity field of NGC 5953 with the HST *V*/*R* image, shows that the rising part of the receding side of the curve (marked *E* in Fig. 11) corresponds to a sector of double velocity profiles. On the approaching side of the curve, the points with minimum $V_{\rm rot}$ (points between 10 and 13″, marked *F* in Fig. 11) correspond to a region closer to the companion on the plane of the sky. The region of the flocculent pattern can be associated with the rising part of the curve and with the turn-off point of the curve where a small bump is observed (marks A and B in Fig. 11). The flat and symmetrical part of the curve corresponds to the main body of the underlying disk beyond the region where the flocculent arms are found (marked D in Fig. 11).

A representative maximum $V_{\rm rot}$ is reached at ∼4″ (0.52 kpc) from the center, with a value of (218 ± 10) km s^{-1}, similar to the value reported by Reshetnikov (1993) and lower than that reported by González-Delgado & Perez (1996) (240 km s^{-1}).

3.6.5. NGC 5954 rotation curve

The rotation curve was computed considering an angular sector of 35° on each side of the representative major axis for this galaxy. A PA of (357 ± 1)°, an inclination of (67.5 ± 2)° and a systemic velocity of $V_{\rm syst}$ = 1856.0 km s^{-1} were chosen, giving a symmetric curve with the least scatter.

The resulting [N II] Fabry-Perot rotation curve for NGC 5954 (KPG 468B) is shown in the upper panel of Fig. 12. The lower panel shows the superposition of both branches.

Solid body rotation is detected within the inner 5″. The rotation curve then reaches a symmetric plateau between 5″ and 25″ (last emission point on the approaching side) with $V_{\rm rot}$ ∼ 105 km s^{-1}. For the receding side (farther from the companion), the curve remains globally flat from 5″ out to 31″. After this point, the curve shows an important bump between 31″ and 36″ where the rotational velocity goes from 105 km s^{-1} to 142 km s^{-1} at 33.3″ and then down

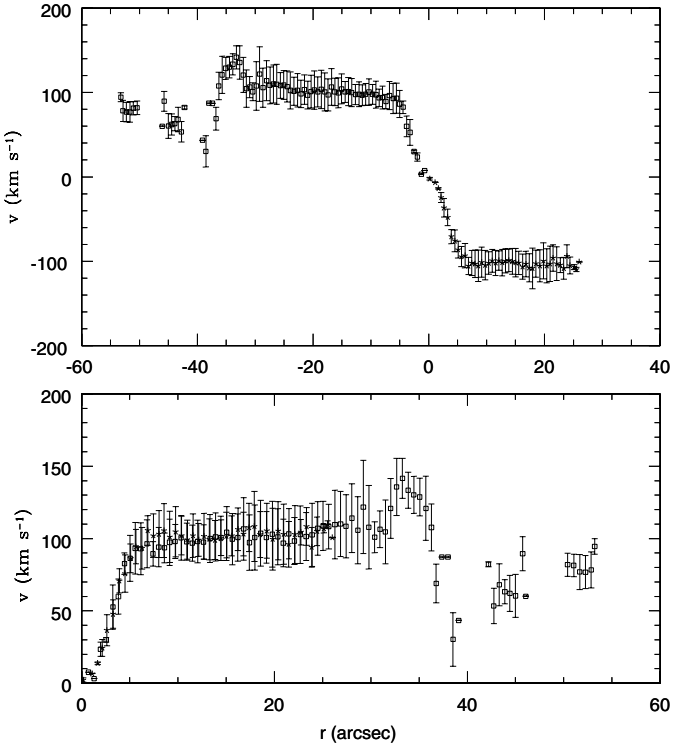

Fig. 12. [N II] rotation curve for NGC 5954.

to 108 km s^{-1} at 36″. From this radius onwards, the velocities oscillate considerably decreasing dramatically (down to ∼31 km s^{-1} at 38″ from the center. Velocity data (between 30 and 95 km s^{-1} could be detected up to ∼53″. This strong velocity oscilation is discussed in Sect. 4.1.

A representative maximum rotational velocity ((112 ± 10) km s^{-1}) is reached at 26″ (3.3 kpc) for the approaching side and at a radius of 32″ (4.1 kpc) for the receding side. This value for $V_{\rm max}$ is close to $V_{\rm max}$ = 130 km s^{-1} reported by Reshetnikov (1993). Notice the peculiar nature of the rotation curve of the gas due to the truncated velocity field on the southwestern side and the displacement to the southwestern of the symmetry axis of the central part of the curve with respect to the barycenter of the star light. This is consistent with the spectroscopic results by Rampazzo et al. (1995).

A closer association of the rotation curve of NGC 5954 with particular features on the composite resolution [N II] image, shows that the region where the rotation curve remains flat up to 31″ on the receding side can be associated with a region between the southern and the northern bubble-like features at the north of the galaxy. The end of the bump (∼36″) matches the region on the northern [N II] tail where the radial velocity reaches a maximum. This region is also associated with the northwestern edge of the northern bubble-like feature. The points with smaller rotational velocities (≤95 km s^{-1}) fall on the tip of the [N II] tail.

Previous values for systemic velocities and kinematical parameters including the values estimated in this work are shown in Table 4.

Table 4. Kinematical data for NGC 5953/54.

Galaxy	NGC 5953	NGC 5954	References
Systemic velocity	2164 ± 35	2123 ± 35	Page (1970)
-heliocentric (km s^{-1})	2037 ± 43	1945 ± 39	Turner (1976)
		(HI) 2000	Shostak (1978)
		(HI) 1935	Haynes (1981)
	(HI) 1950 ± 75	(HI) 1969 ± 75	Bottinelli et al. (1981)
		2013	Tifft (1982)
	1983 ± 28	2012 ± 28	White et al. (1983)
		(HI) 1938	Davies & Seaquist (1983)
		(HI) 1848	Davies & Seaquist (1983)
		(HI) 1955 ± 16	Giovanardi & Salpeter (1985)
		(HI) 1960	Lewis et al. (1985)
	(HI) 1864	(HI) 1864	Armstrong & Wootten (1986)
	(HI) 1964	(HI) 1971	Garwood et al. (1987)
	2100 ± 30		Rafanelli et al. (1990)
	1994 ± 14	1848 ± 14	Reshetnikov (1993)
	1987 ± 10	1883 ± 11	Rampazzo et al. (1995)
	Hα,[N II],[SII] 1870 ± 36	Hα,[N II],[SII] 1907 ± 11	Rampazzo et al. (1995)
	[N II] 1962 ± 10	[N II] 1856 ± 10	This work
Inclination i (°)	25 ± 5	61 ± 2	Reshetnikov (1993)
	45	63	LEDA
		65 ± 3	Rampazzo et al. (1995)
	25 ± 5		González-Delgado & Pérez (1993)
	32 ± 2	67.5 ± 2	This work (Kinematics)
	34 ± 7	60 ± 7	This work (Photometric)
PA (north eastwards) (°)	151	5	LEDA
	169	5	RC3
		3	Rampazzo et al. (1995)
	39	355	Reshetnikov (1993)
	51		González-Delgado & Pérez (1993)
	51 ± 10	357 ± 10	This work (Kinematics)
	45 ± 7	3 ± 7	This work (Photometric)
Maximum rotational velocity	200	130	Reshetnikov (1993)
(km s^{-1})	240		González-Delgado & Pérez (1993)
	218 ± 10	112 ± 12	This work

3.7. Mass estimates

Observations and simulations of encounters show that for interacting disk galaxies perturbations tend to go from the outer part of the disk to the central regions according to the stage of the interaction. Assuming that NGC 5953/54 is suffering a moderate interaction, circular motion of the gas presumably dominate in the inner regions, such that up to a certain radius, the rotation curve is valid and representative of the bulk motions in each galaxy. In order to determine this radius, we looked for the point on the rotation curves where symmetry is dramatically lost ($|V_{\rm receding} - V_{\rm approaching}| \geq 30$ km s^{-1}) or

Table 5. Mass estimations for NGC 5953/54.

Galaxy	NGC 5953	NGC 5954
$R_{\rm sym}$ in kpc	1.3	3.3
$V(R_{\rm sym})$ in km s^{-1}	180	112
$R_{25}/4$ in kpc	1.7	1.6
$V(R_{25}/4)$ in km s^{-1}	190	108
Mass within $R_{\rm sym}$ ($M_\odot$)	9.4×10^9	9.3×10^9
Mass within $R_{25}/4$ ($M_\odot$)	1.4×10^{10}	4.1×10^9

where there is an abrupt variation in the velocity such that $\Delta V > 50$ km s^{-1} in less than 0.1 R_{25}.

For NGC 5953, our F-P observations go as far as 26″ (3.35 kpc). Symmetry between both sides is drastically lost at $R_{\rm sym}$ = 10.2″ (1.31 kpc) where the velocities on the approaching side (the one closer to the companion) start decreasing. For the receding side, notice that the curve remains almost flat up to 12.5″ (1.6 kpc).

For NGC 5954, F-P observations go as far as 53″ (6.8 kpc). Symmetry is preserved between the two sides out to $R_{\rm sym}$ = 26″ (3.3 kpc) on the approaching side. However, notice that the curve remains almost flat out to 32″ (4.1 kpc) on the receding side.

Once we had established $R_{\rm sym}$, a first estimate of the mass (by equating the gravitational force with the centrifugal force; $M(R) = (RV^2(R))/G$ in the case of a spheroidal distribution of mass) was carried out. Notice that the accuracy in this estimate is ∼50% for a mass distributed in a disk. The mass estimations for each galaxy are presented in Table 5.

From Table 5 we notice that $R_{\rm sym}$ is a factor 2.5 lower for NGC 5953 than for NGC 5954, while the rotational velocity at $R_{\rm sym}$ is a factor 1.6 greater for NGC 5953 than for NGC 5954. The result in this case, illustrates the danger of comparing kinematical masses at a non-standar radius. However, as an attempt to do a fair comparison, we have estimated (from our photometry) the radius at the 25 mag/″^{2} B-band isophote (R_{25}) for each galaxy and calculated the kinematical masses at one-fourth the optical radius. In this way, NGC 5953 appears about 3 times more massive than NGC 5954, consistent with the observed difference in amplitude of the maximum rotational velocities in these galaxies. From Table 5 the spatial extension of the optical underlying stellar disk in NGC 5953 can be inferred, emphasizing the strong spatial confinement of the [N II] emission in this galaxy.

4. Discussion

4.1. Kinematics

We discuss some aspects of the internal kinematics of NGC 5953/54 from their rotation curves in Figs. 11 and 12 to see if we recognize a pattern that suggests a specific triggering process. The area of solid-body rotation D(SB)/D_{25} for both components was estimated. Since the area of solid-body rotation in a typical disk may depend on the morphological type and on the linear scale of the galaxy, the estimate uses a normalization to the galaxy isophotal diameter in the B-band. The result indicates that the Seyfert component NGC 5953 has typically a smaller area of rising or solid-body rotation than its neighbor Liner galaxy. Extended regions of solid-body rotation have been considered conductive to bar formation, specially in the presence of external perturbations (Noguchi 1988; Shlosman et al. 1989). However, we do not see traces of any barred structure in NGC 5954 at our resolution. On the contrary, for NGC 5953 the HST images reveal the presence of a small 60 pc barred structure.

As an indicator of the relative degree of kinematic disturbances, we use the maximum amplitude of disturbances δv in our rotation curves, relative to a smooth, symmetric form and normalized to the total velocity amplitude $V_{\rm max}$ (thus giving a value indicative of the response to be expected). This value is also indicative of the strength of the total tidal impulse and the time scale over which it has operated. We notice that both members show similar amplitude of kinematic disturbance $\delta v/V_{\rm max}$, from which a similar star formation rate (SFR) can be inferred (Keel 1993), although a significantly higher SFR per unit area is inferred for NGC 5953. This is consistent with other studies in galaxy pairs (Keel 1993) that show an intimate connection between star formation and kinematics. From our morphological and photometric study, it is evident that the two components show different global responses to the interaction process. While NGC 5953 barely shows traces of faint tidal features in Hα and [N II], but instead, a strong spatial confinement of the star formation in its inner region; NGC 5954 shows more extended star formation and morphological disturbances. These differences are furnishing clues that either some particular kind of interaction (orbital properties) and/or, the intrinsic structure of the intervening galaxies might be operating (and perhaps triggering) for the Seyfert and Liner components.

From the [N II] rotation curves, we inferred that NGC 5953 is about 3 times more massive than NGC 5954. Alternatively, from our K-band photometry, a measure of the luminosity ratio can be inferred and thus a mass ratio for NGC 5953/54 can be adopted. Notice from Table 2 that NCG 5953 is systematically brighter at any observed wavelength. This asymmetry is not entirely due to the Seyfert nuclei itself. We have carried out integrations of the analytic component fit to our set of HST images and have found that the maximum point-source contribution to the V/R and H-band integrated light is about 25%. This is similar to estimations for other samples of Seyferts (cf. Kotilainen et al. 1993). It is also not clear how much of this asymmetry in brightness has to do with the interaction and triggering and how much with the fact that the luminosity function of Seyfert host galaxies is weighted toward more luminous systems in general (Meurs & Wilson 1984).

The probability of a galaxy to host a Seyfert nucleus rises rapidly with luminosity, from ∼1% at $M_{\rm B} = -21$ to a value of the order 50% at $M_{\rm B} = -22.5$. This gives a natural bias toward Seyfert nuclei in pairs favoring the brighter member, independent of any contribution from tidal perturbations or internal dynamics. This bias was evaluated by Keel (1996) from an analysis of the power-law distribution of relative magnitudes in the Karachentsev pairs. Thus, considering a typical correction of the order of 20% for the light from the Seyfert

nucleus and a correction $\Delta m \sim 0.25$ for the brighter member bias (at all the observed wavelengths), NGC 5953 still results brighter than NGC 5954, yielding a K-band luminosity ratio $L^K_{\rm NGC\,5953}/L^K_{\rm NGC\,5954} \sim 1.5$. If we assume a similar M/L_K ratio for the two components, the inferred total mass ratio is of the same order, consistent with our kinematical estimate at one-fourth the optical radius. However, notice that adopting the same M/L_K ratio for the two components may be a wrong assumption, especially considering the peculiar morphological nature of NGC 5953. A mass ratio for NGC 5953/54 ~ 2 will be adopted in the following discussion. This result is also consistent with the fact that interactions may trigger activity more efficiently in more luminous galaxies, beyond the known relation between galaxy luminosity and probability of hosting an AGN.

4.2. Morphology and simulations

The interpretation of the observed morphology can give significant clues to the orbital properties, in concert with numerical simulations. The symmetry of tidal distortion and whether any tails are broad or narrow prove to be powerful tests. Direct encounters produce rather narrow bridges and tails, while those due to a retrograde passage are more fan-like. On the other hand, planar encounters, especially with light haloes, give the most symmetric response, with the average symmetry between bridge and tail structures decreasing to higher orbital inclination.

We use a "dictionary" of simulations of tidally induced structures in disk galaxies that covers many encounter parameters with fine morphological resolution and including effects of self-gravitation, presented by Howard et al. (1993).

We will be considering, in a first approximation, a morphological matching between our observed galaxies and a frame in this dictionary as a determination of some parameters of the encounter assuming the implicit model for the galaxy and halo as specified in the Howard et al. (1993) simulations. Matching the disk morphology has a higher priority than matching the projected position and radial velocity of the companion due to the uncertainty introduced by the extent and form of the halo in these simulations. Thus in this dictionary, the time since close approach, the close approach distance, the relative mass, the orbital inclination and the sense relative to the disk, along with the halo to disk ratio will specify the encounter.

The available observational constraints are 1) the relative PAs of galaxy disks, 2) the disk inclination of both components, 3) the relative velocities, 4) the disks rotation direction, and 5) the form of any tidal disturbances noted on the images. Distortion of either pair member is direct evidence that the galaxies are physically connected.

Figure 13 summarizes some of the main features detected in NGC 5953/54 from our observations as follows:

1) NGC 5953 has a spiral flocculent pattern concentrated in its first 12″ (confirmed from HST images), seen as a strong circumnuclear starburst within 1.5 kpc in our low-resolution images. An extended disk is detected at all the observed wavelengths but no trace of underlying structure beyond 2 kpc was detected, except for a cloud-like (envelope?) suggested from the a_4/a profile and a fan-like two-sided tide visible in the Hα and [N II] images beyond 25″. In addition, the HST images show evidence of a possible barred central (~60 pc) structure. The fact that this galaxy hosts a Seyfert 2 nucleus reminds us about the role that the observed inner spiral pattern could be playing to transport angular momentum from the center to the outer parts, as in the case of trailing patterns (e.g. Combes 2001). Following this idea, we tentatively assume the western side of NGC 5953 as the near side in order to have an inner trailing pattern.

2) The Liner galaxy NGC 5954 is a strongly disturbed blue spiral where the northern part shows evidence of a) two large bubble-like structures with double [N II] Fabry-Perot profiles associated with the southern-most structure; b) a circumnuclear and also a more extended starburst all along the disk; c) a northwestern spiral arm that could be interpreted as a tidal arm which runs northwards and to the west of the main disk and that probably lies near the disk plane; d) a high-contrast arm-interarm region visible in all the observed bands (probably an interaction-induced density wave arm); e) a faint curved tail in [N II] of tidal origin about 30″ long and extending to the north; f) a bridge (detected in all the observed bands) apparently connecting this pair that could be interpreted as tidally generated structure that runs to the south of NGC 5954, twisting of the disk plane and turning west to form the stellar bridge (the color maps favor this interpretation). We suggest that the plume northwest of NGC 5953 is an extension of the bridge emerging from NGC 5954. NGC 5954 appears as an eye-shaped oval with a double parallel arm structure in the J and K-band images. This may be interpreted as g) a tidal tail and a streaming arm on the side close to the companion.

3) From the B-band and Hα imaging, the majority of the brightest H II regions in NGC 5954 are apparently in the far side with respect to NGC 5953. However, from the J and K-band images the appearance of the galaxy is more symmetric in brightness. Thus, the apparent asymmetry in the H II distribution may be due in part to an inclination effect, suggesting that the near side of NGC 5954 could be the western side.

4) In the bridge region, the B-band emission at different brightness levels lies to the south with respect to the [N II] emission. This offset could be reflecting the motion of the perturbation in that region.

5) We adopt a mass ratio of 2 for NGC 5953/NGC 5954.

We assume that all features observed in NGC 5953/54 lie near the disk planes. Combining the information for inclinations, corresponding velocity fields and the assumptions about which side is closer to us, it is suggested that NGC 5953 and NGC 5954 are rotating in opposite senses arround their individual axis. Since tides are two-sided features, given the observed asymmetry of the tides in NGC 5954, NGC 5953 is suggested to be moving in a direct (inclined) orbit with respect to the disk of NGC 5954. This implies that, viewed from NGC 5953, NGC 5954 is moving in a retrograde orbit.

A careful look at the dictionary of simulations was carried out, taking into account a moderate tilt from face-on of the galaxy being matched or of a difference in position angle of the arms compared to the matching simulation frame. We have analyzed direct and retrograde encounters, for each component

Table 6. Parameters of encounters for KPG 468 (NGC 5953/54) from the Atlas of simulations of Howard et al. (1993).

Simulation	Sense	i	M_P/M_g	r_{min}/R_g	H/D
NGC 5954					
20	Direct	30	0.5	1.0	10
21	Direct	30	1.0	1.0	10
32	Direct	60	0.5	1.0	10
33	Direct	60	1.0	1.0	10
NGC 5953					
38	Retrograde	0	0.5	1.0	1
39	Retrograde	0	1.0	1.0	1
44	Retrograde	0	0.5	1.0	10
45	Retrograde	0	1.0	1.0	10

separately assuming: 1) A grazing passage where r_{min}/R_g is the periapsis of an initial parabolic orbit, in units of the initial disk radius. In terms of the radius of the Mestel disk, R_g, the closest approach value is 1 for a grazing passage, 2) a mass ratio of 0.5 (we also explored a value of 1) where the ratio is of total companion mass to total (disk + halo) mass of the primary, and 3) different orbit inclinations.

Table 6 reports the numbers and main characteristics of Howard et al. (1993) simulations that qualitatively match the observed morphology in NGC 5953 and NGC 5954.

Numerical simulations show that planar direct encounters are especially effective at mass transfer, with all but the low-mass distant companions collecting disk particles. However, as emphasized in Howard et al. (1993), a more careful analysis is needed at higher inclinations because their dictionary of encounters is such that particles are not allowed to follow the companion out of the plane. Jenkins (1984) modelled the encounter of NGC 5953/54 suggesting a polar parabolic encounter of initial separation ~20 kpc, minimum separation ~5 kpc, time $t \sim 4 \times 10^7$ yr from closest approach, with no evidence of transfer of material. We found however, no polar encounter that could qualitatively match the observed morphology in NGC 5954.

Alternatively, simulations 20, 21, 32 and 33 in Table 6 were chosen as tentative scenarios to explain the observed morphology of NGC 5954. From these direct, inclined ($30° \leq i \leq 60°$) encounters, some features can be interpreted: (a) The filamentary (bubble-like) structures at the north of NGC 5954 as well as the inter-arm region and the almost parallel arms (J and K-band images) at the northwest as due to the crowding of the stellar an gas orbits, (b) the bridge and plume (seen at northwest of NGC 5953) as a tidal structure generated from the gas and stars in NGC 5954 and (c) the intrinsically oval shape of the inner and intermediate regions as inferred from the geometric profiles and the near-IR images. These encounters also suggest that NGC 5953 may have cross-fuelled some material from NGC 5954 while crossing at its early closest passage.

For NGC 5953, it is more difficult to find plausible scenarios due to the absence of clear morphological features to match. However, from the observed morphology, photometric results and the inferred orbital geometry for NGC 5954, the retrograde planar simulations 38, 39, 44 and 45 in Table 6 were selected as tentative scenarios. These simulations suggest that NGC 5953 may have suffered a redistribution of its original structure (gas and stars) after a closest approach, leaving (a) a crowding of stars and compressed gas in a ring-like inner central region, from which a starburst event may be expected, consistently with the observations, and (b) a smooth structureless underlying external region and a kind of scattered material envelope, resembling an S0-like/early-type morphology. Assuming this scenario as plausible, the presence of an inner flocculent pattern may be suggesting a secularly evolved morphology for NGC 5953 via the interaction with NGC 5954.

Notice that the selected simulations are consistent in the sense that they suggest: 1) the expected mass of companion to primary, 2) similar mass of halo to disk of the primary, 3) similar time step interval (250−500 in simulation units) and 4) similar grazing encounters.

4.3. NGC 5953/54: A pair of mutually triggered AGNs?

Galaxy interactions can be the most efficient way to produce strong torques, and to transfer away the angular momentum. Strong non-axisymmetric forces are exerted on the gas, but contrary to what could be expected, the main torques responsible for the gas inflow are not directly due to the companion. The tidal perturbations destabilize the intervening disks and the non-axisymmetric structures generated (bars, spirals) are responsible for the torques. The self-gravity of a disk and its consequent gravitational instabilities, play the fundamental role. The internal structure therefore takes over from the tidal perturbations on the outer parts. The gas may be provided by the galaxy itself but another possibility could be that the gas accreted from the companion is the main trigger for activity.

If a central bulge already exists, this tends to stabilizes the disk with respect to external perturbations. If the bulge is sufficiently massive, the apparition of non-axisymmetries is delayed and so are the gas inflow and the consequent star-formation activity. But the starburst would then be stronger. When the galaxy is of late type, without any bulge, the gravitational instability settles in at an early stage of the interaction. There is then a continuous activity during the interaction, but at the end the starburst would be less violent, since a fraction of the gas has already been progressively consumed before.

On line with the above scenario and assuming for NGC 5954 a late-type morphology previous to the encounter, it is reasonable to expect broadly extended star formation activity throughout its disk. This is consistent with our observations. In this scenario, the bubble-like features to the north may be considered as footprints of intense star formation. However, as shown in the simulations, these features can be reproduced by the crowding of the stellar and gaseous orbits during the encounter. The selected simulations also show crowding of the stellar and gaseous components in the inner region, consistent with the prominent circumnuclear starburst observed.

For NGC 5953, the selected simulations suggest that the retrograde encounter in NGC 5953 could have drastically transformed its pre-encounter morphology, producing a strong concentration of both gas and stars in the inner regions. This is consistent with our kinematic study that suggests considerable mass contained in its inner regions. Furthermore, NGC 5953 has a substantial amount of molecular gas ($\sim 10^{8.8}$ $M_{\odot}$ within the central 33″, Wilkind & Henkel 1989), and slightly less than half this amount within the central 15″, according to Sofue et al. (1993). These facts favor the presence of strong inner star formation, as observed. The evidence for cross-fuelling is fairly weak from the selected simulations.

From this preliminary analysis, any direct mechanism that relates the inferred geometry of the encounter to the presence of the Seyfert/Liner activity in NGC 5953/54 remains elusive.

5. Conclusions

In this paper, photometric (*BVRIHαJK*), morphological, and [N II] kinematic observations are presented and reviewed to visualize the effect of the encounter on the motions, and distribution of the gas and stars in the galaxy pair NGC 5953/54. From our analysis, some tentative orbital properties of the encounter have been inferred, with the aim of finding features that might give clues to whether and how an AGN can be triggered by galaxy interactions. As evidenced from our observations, the role of large-scale dynamics and interactions of galaxies is more straightforward for the starburst activity. However, as assumed in this paper, if the AGN activity is being triggered in pairs by any particular mechanisms, then these mechanisms, whatever they are, are equally prone in prograde and retrograde encounters.

The scenario emerging from matching the observed morphology to simulations emphasizes the fundamental role that both the interaction geometry and the intrinsic structure of the intervening galaxies can play in the morphological transformation of NGC 5953/54. The assumed early-type component (NGC 5953) is currently seen hosting a probable interaction-induced inner flocculent pattern. Furthermore, the underlying disk (seen in our optical and near-IR observations) may be the remnant of its pre-encounter morphology. There is weak evidence that cross-fuelling may have occurred in earlier stages of the encounter. NGC 5953/54 may have suffered a secular transformation via the interaction process.

We emphasize that the interpretation based on the selected simulations is clearly tentative. This attempt to match the observed morphology helps us to understand the geometric nature of the encounter in NGC 5953/54 and allows us to gain insight about how the interactions may be causing or stimulating the star formation and nuclear activity, as originally deviced in our working hypothesis.

Clear strategies for further work in this direction will be higher s/n full mapping of the velocity fields, using the VLA or optical line emission, and more precise understanding of the geometry and orbits of paired galaxies, with velocity maps coupled to n-body simulations. Such studies will lead to improved understanding of the time scales involved, and what are the most promising physical processes to account for nuclear activity enhancing in paired galaxies. On line with this strategy, a forthcoming paper is devoted to a more detailed analysis of our observations, including HI synthesis observations coupled with our n-body simulations.

Acknowledgements. The authors thank the night assistants G. Garcia, F. Montalvo, S. Monroy and the staff of the Observatorio Astronomico Nacional (OAN-SPM) for their valuable help during the observations. H. H. T. thanks L. Olguín and J. A. García-Barreto for their encouraging comments. M. R. acknowledges support through grant IN120802 from DGAPA, UNAM.

References

Alfaro, E. J., Pérez, E., González-Delgado, R. M., Martos, M. A., & Franco, J. 2001, ApJ, 550, 253
Andersen, D. R., & Bershady, M. A. 2002, in ASP Conf. Proc. 275, ed. E. Athanassoula, A. Bosma, & R. Mújica, ISBN: 1-58381-117-6 (San Francisco: Astronomical Society of the Pacific), 39
Armstrong, J. T., & Wooten, H. A. 1986, Astrophys. Sp. Sci. Lib., 124, 439
Barnes, J. E., & Hernquist, L. 1992, ARA&A, 30, 705
Barnes, J. E., & Hernquist, L. 1996, ApJ, 471, 115
Barton, J. E., Bromley, B. C., & Geller, M. J. 1999, ApJ, 511, L25
Bergvall, N., & Johansson, L. 1995, A&AS, 113, 499
Bottinelli, L., Gouguenheim, L., & Paturel, G. 1981, A&AS, 44, 217
Carrasco, L., Garcia-Barreto, A., Recillas-Cruz, E., Cruz-González, I., & Serrano, A. 1991, PASP 103, 987
Chengalur, J. N., Salpeter, E. E., & Terzian, Y. 1994, AJ, 107, 1984
Combes, F. 2001, in Advaced Lectures on Starburst-AGN Connection, ed. I. Aretxaga, D. Kunth, & R. Mújica, 223
Cruz-González, I., Carrasco, L., Ruiz, E., et al. 1994, RMxAA, 29, 197
Cutri, R. 1990, IAU Coll., 124, 415
Dahari, O. 1984, AJ, 89, 966
Davis, L. E., & Seaquist, E. R. 1983, ApJS, 53, 269
Domingue, D. L., Sulentic, J. W., Xu, C., et al. 2003, AJ, 125, 555
Dultzin-Hacyan, D., Krongold, Y., Fuentes-Guridi, I., & Marziani, P. 1999, ApJ, 513, L111
de Jong, R. S. 1996, A&A, 313, 377
de Vaucouleurs, G., de Vaucouleurs, A., Corwin, H. G., et al. 1991, Third Reference Catalogue of Bright Galaxies (New York: Springer-Verlag)
de Vaucouleurs, A., & Longo, G. 1988, Catalogue of visual and infrared photometry of galaxies from 0.5 μm to 10 μm, University of Texas
Edelson, R. A., & Malkan, M. A. 1986, ApJ, 308, 59
Elmegreen, B. G., Sundin, M., Kaufman, M., Brinks, E., & Elmegreen, D. M. 1995, ApJ, 453, 139
Franco-Balderas, A., Hernández-Toledo, H. M., Dultzin-Hacyan, D., & García-Ruiz, G. 2003, A&A, 406, 415
Fuentes-Carrera, I., Rosado, M., Amram, P., et al. 2003, A&A, in press
Garwood, R. W., Helou, G., & Dickey, J. M. 1987, ApJ, 322, 88
Gezari, D. Y., Schmitz, M., Pitts, P. S., & Mead, J. M. 1993, Catalog of IR Observations, third ed., NASA RP-1294
Giovanardi, C., & Salpeter, E. E. 1985, ApJS, 58, 623
González-Delgado, R. M., & Pérez, E. 1996, MNRAS, 281, 781
Haynes, M. P., & Giovanelli, R. 1984, AJ, 89, 758
Haynes, M. P. 1981, AJ, 86, 1126
Henriksen, M., & Cousineau, S. 1999, ApJ, 511, 595
Hernández-Toledo, H. M., Dultzin-Hacyan, D., González, J. J., & Sulentic, J. 1999, AJ, 118, 108

Hernández-Toledo, H. M., Dultzin-Hacyan, D., & Sulentic, J. 2001, AJ, 121, 1319
Hernández-Toledo, H. M., & Puerari, I. 2001, A&A, 379, 54
Hernández-Toledo, H. M., Avila-Reese, V., & Sulentic, J. 2003, in preparation
Hibbard, J. E., Guhatakurta, P., van Gorkom, J. H., & Schweizer, F. 1994, AJ, 107, 67
Howard, S. A., Keel, W. C., Byrd, G. G., & Burkey, J. M. 1993, ApJ, 417, 502
Hunt, L. K., Mannucci, F., Testi, L., et al. 1998, AJ, 115, 2594
Hunt, L. K., Malkan, M. A., Rush, B., et al. 1999, ApJS, 125, 349
Jenkins, C. R. 1984, ApJ, 277, 501
Johansson, L., & Bergvall, N. 1990, A&AS, 86, 167
Joseph, R. 1982, MNRAS, 209, 111
Karachentsev, I. D. 1972, Catalogue of Isolated Pairs of Galaxies in the Northern Hemisphere, Comm. Spec. Ap. Obs., 7, 1
Karachentsev, I. D. 1987, Double Galaxies (Moscow: Nauka)
Kaufman, M., Brinks, E., Elmegreen, B. G., et al. 1999, AJ, 118, 1577
Kennicutt, R. C. 1983, ApJ, 272, 54
Knapen, J. H., & van der Kruit, P. C. 1991, A&A, 248, 57
Keel, W. C., Kennicutt, R. C., Hummel, E., & van der Hulst, J. M. 1985, AJ, 90, 708
Keel, W. C. 1996, AJ, 111, 696
Kotilainen, J. K., Ward, M. J., & Williger, G. 1993, MNRAS, 263, 655
Kotilainen, J. K., & Ward, M. J. 1997, A&AS, 121, 77
Landolt, A. U. 1992, AJ, 104, 340
Lewis, B. M., Helou, G., & Salpeter, E. E. 1985, ApJS, 59, 161
Malkan, M. A., Gorjian, V., & Tam, R. 1998, ApJS, 117, 25
Meurs, E. J. A., & Wilson, A. S. 1984, A&A, 136, 206
Milvang-Jensen, B., & Jørgensen, I. 1999, Baltic Astron., 8 535
Mirabel, I. F., Lutz, D., & Maza, J. 1991, A&A, 243, 367
Mulchaey, J. S., Wilson, A. S., & Tsvetanov, Z. 1996, ApJ, 467, 197
Nilson, P. 1973, Uppsala General Catalogue of Galaxies, Uppsala Astr. Obs. Annaler, Band 6
Noguchi, M. 1988, A&A, 203, 259
Noguchi, M. 1990, in Paired and Interacting Galaxies, IAU Coll., 124, 711
Oke, J. B., & Gunn, J. E. 1983, ApJ, 266, 713
Page, T. 1970, ApJ, 159, 791
Pismis, P. 1988, Lecture Notes in Physics, ed. L. Blitz, & F. J. Lockman (Springer-Verlag), 306, 61
Rafanelli, P., Osterbrock, D. E., & Pogee, R. W. 1990, AJ, 99, 53
Rampazzo, R., Reduzzi, L., Sulentic, J. W., & Madejsky, R. 1995, A&AS, 110, 131
Regan, M., & Elmegreen, D. M. 1997, AJ, 114, 965
Reshetnikov, V. P. 1993, A&A, 280, 400
Roberts, M. S., & Haynes, M. P. 1994, ARA&A, 32, 115
Rosado, M., Langarica, R., Bernal, A., et al. 1995, RMxAAC, 3, 263
Rosado, M., Valdéz-Gutiérrez, M., Georgiev, L., et al. 2001, AJ, 122, 194
Sérsic, J. L., & Pastoriza, M. 1965, PASP 77, 287
Shlosman, I., Frank, J., & Begelman, M. 1989, Nature, 338, 45
Shlosman, I. (ed.) 1994, Mass-Transfer Induced Activity in Galaxies (Cambridge University Press)
Shostak, G. S. 1978, A&A, 68, 321
Sofue, Y. 1993, PASP 105, 308
Sofue, Y., Wakamatsu, K., Taniguchi, Y., & Nakai, N. 1993, PASJ, 45, 43
Tifft, W. G. 1982, ApJS, 50, 319
Toomre, A., & Toomre, J. 1972, ApJ, 178, 623
Turner, E. L. 1976, ApJ, 208, 20
Visser, H. C. D. 1980, A&A, 88, 149(159)
Wiklind, T., & Henkel, C. 1989, A&A, 225, 1
White, S. D. M., Huchra, J., Latham, D., & Davis, M. 1983, MNRAS, 203, 701
Yoshida, M., Yamada, T., Kosugi, G., Taniguchi, Y., & Mouri, H. 1993, PASJ, 45, 761

Online Material

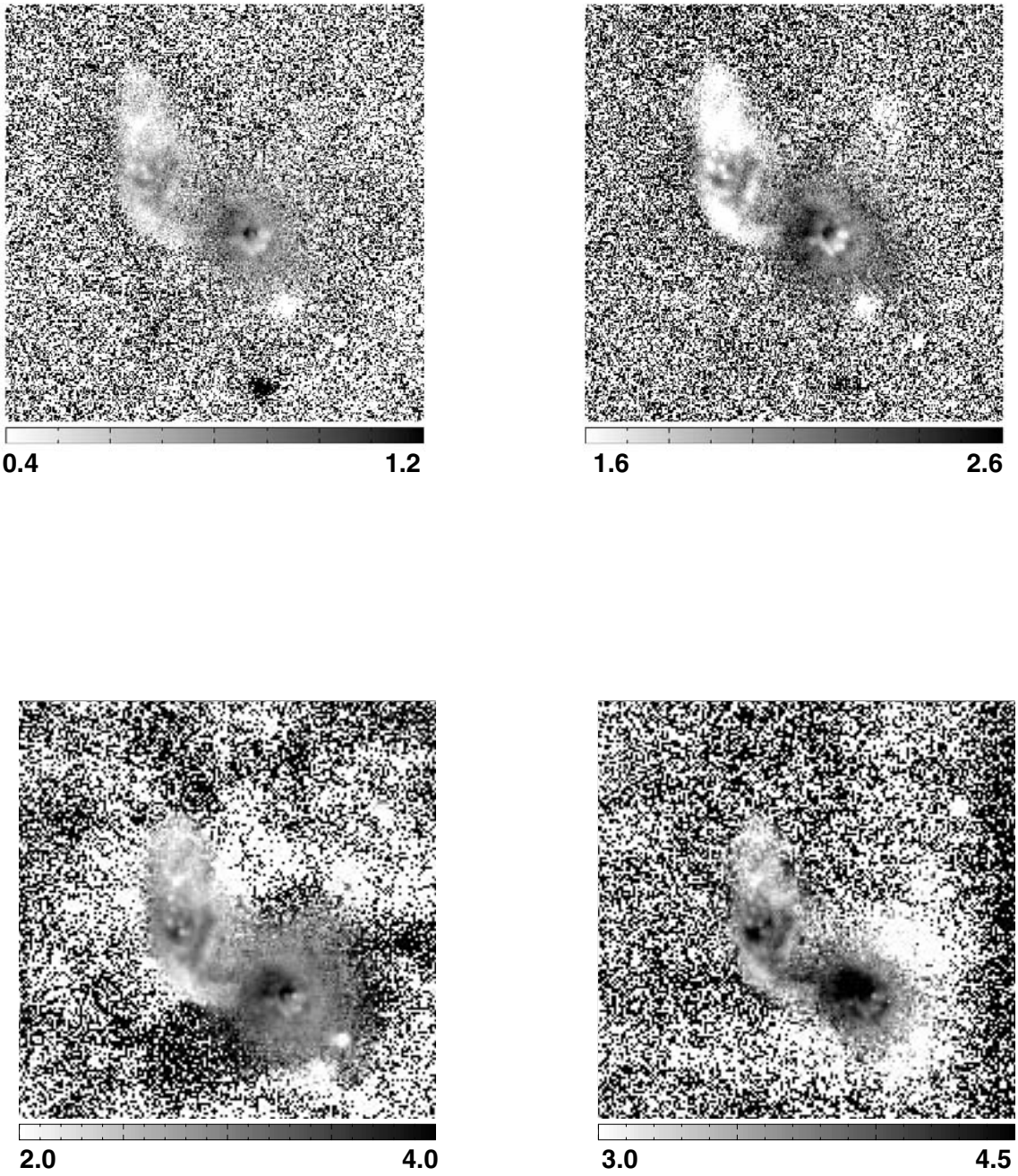

Fig. 5. NGC 5953/54. *Top left*: $B - V$ color index map. *Top right*: $B - I$ color index map. *Bottom left*: $B - J$ color index map. *Bottom right*: $B - K$ color index map.

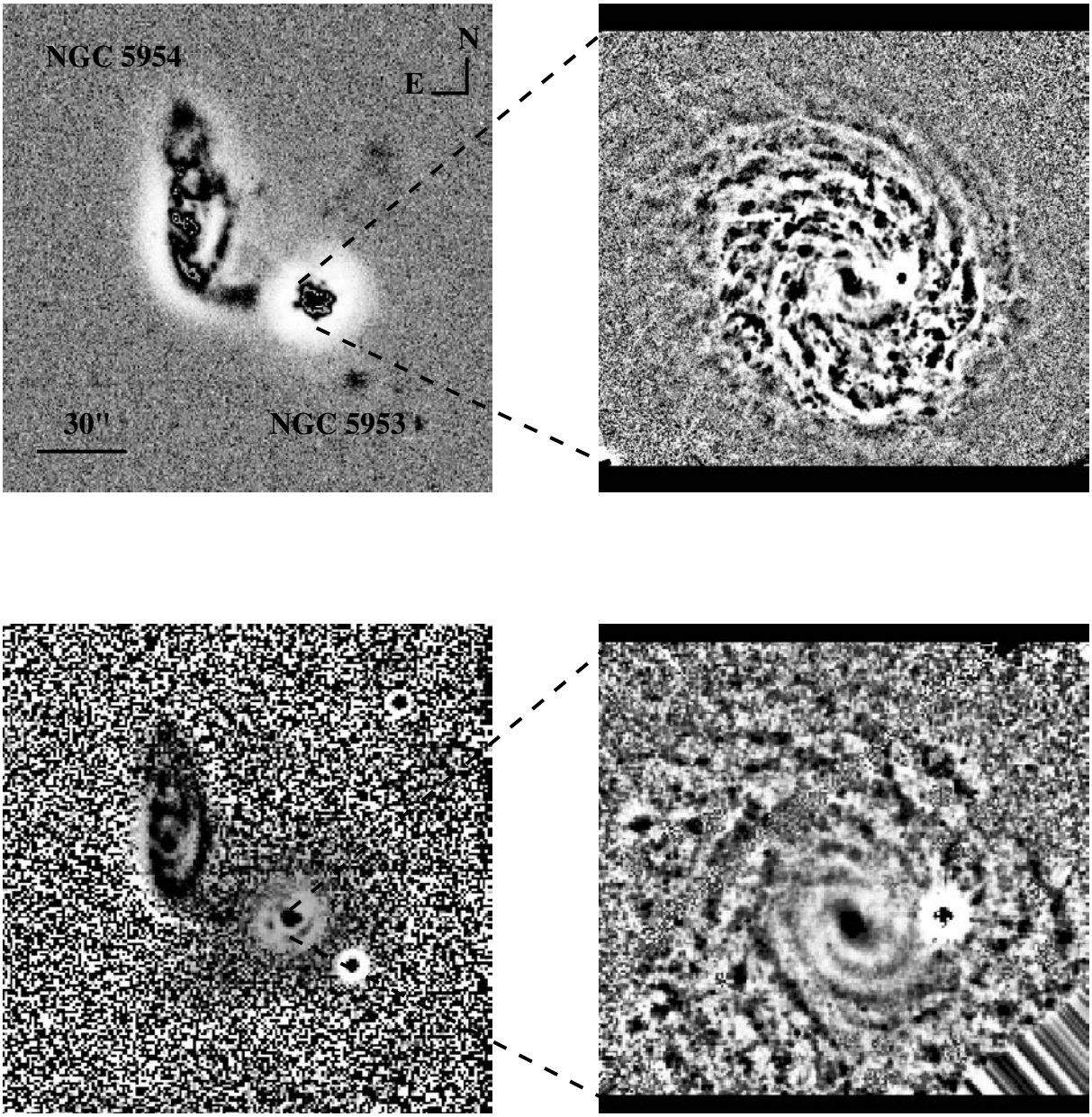

Fig. 7. *Upper panel*: 1.5-m contrast-enhanced *B*-band image of NGC 5953 and a zoom of the corresponding central region as viewed from the (*V*/*R*) band WFPC2 in HST. *Lower panel*: 2.1-m contrast enhanced *J*-band image and a zoom of the central region as viewed from the *H*-band NICMOS in HST. Contrast-enhancing was applied to both *V*/*R* and *H*-band images from HST. All the images are oriented according to the astronomical convention.

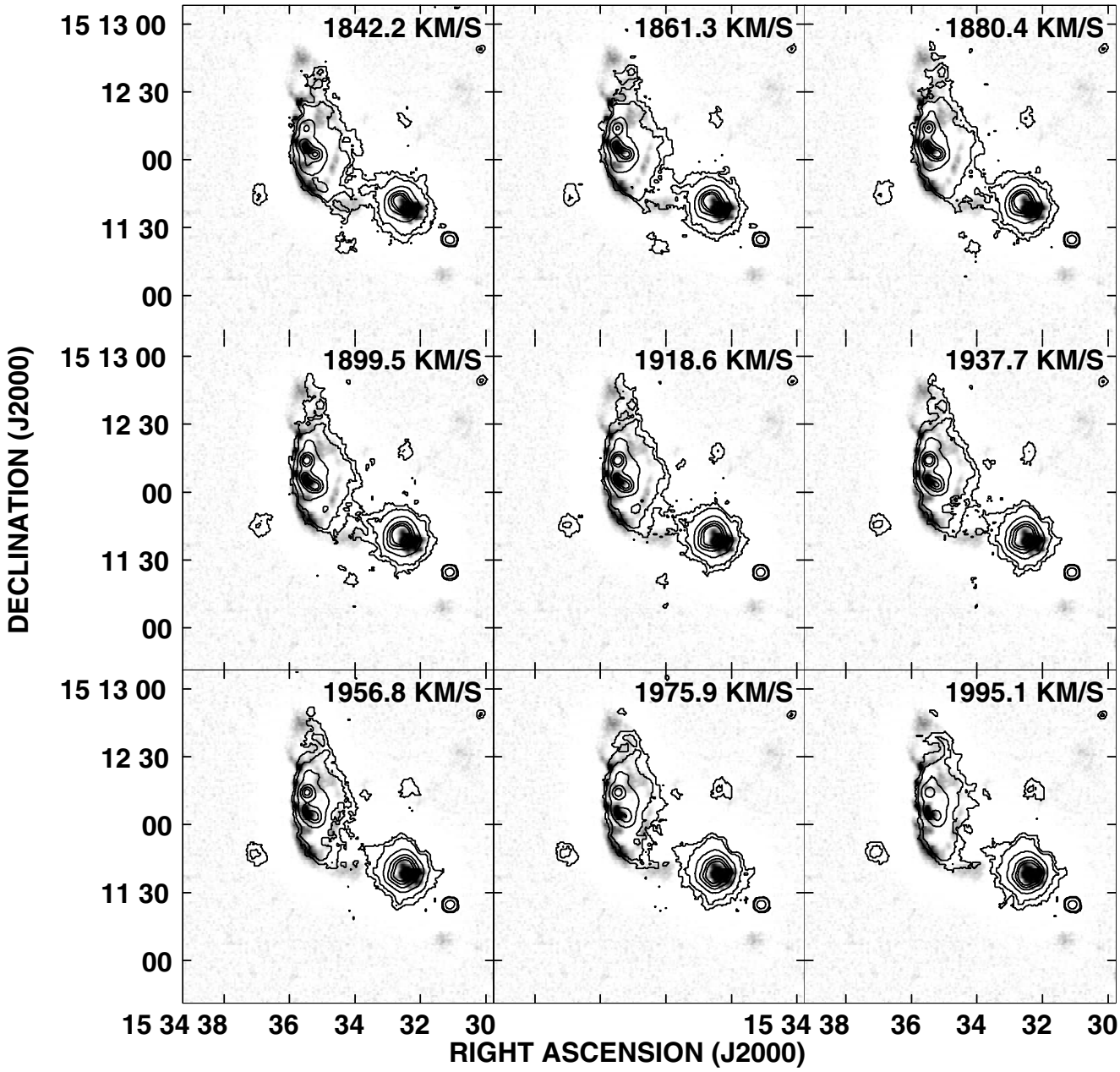

Fig. 10. Set of channel maps from the raw [N II] cube overlaid on a gray-scale display of our *B*-band contrast-enhanced image. The contour levels are 0.97, 1.15, 2, 4, 6, and 8 times the rms noise.

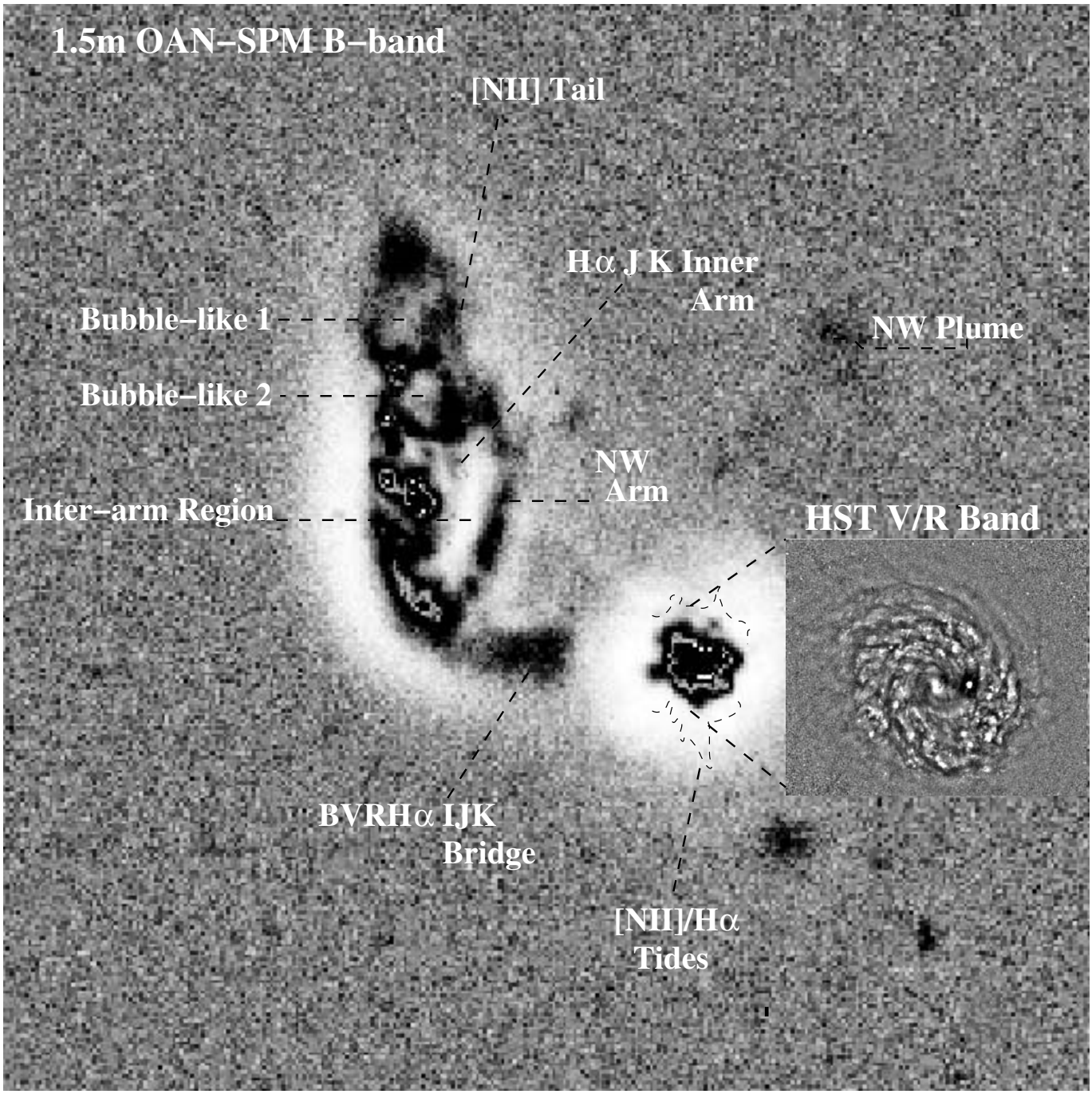

Fig. 13. 1.5-m OAN-SPM *B*-band contrast-enhanced image showing a schematic representation of the observed features in NGC 5953/54. $1'' = 0.13$ kpc yielding a projected separation of ~5.8 kpc. A zoom of the central parts of NGC 5953 with the Hubble Space Telescope *V*/*R* band image is also shown.